Report
R-17-04
January 2018

Use of infrared pictures to assess flowing channel frequencies and flowrates in fractured rocks

A feasibility study

Ivars Neretnieks
Luis Moreno
Longcheng Liu
Batoul Mahmoudzadeh
Pirouz Shahkarami
Olga Maskenskaya
Pär Kinnbom

SVENSK KÄRNBRÄNSLEHANTERING AB

SWEDISH NUCLEAR FUEL
AND WASTE MANAGEMENT CO

Box 3091, SE-169 03 Solna
Phone +46 8 459 84 00
skb.se

SVENSK KÄRNBRÄNSLEHANTERING

ISSN 1402-3091
SKB R-17-04
ID 1578278
January 2018

Use of infrared pictures to assess flowing channel frequencies and flowrates in fractured rocks

A feasibility study

Ivars Neretnieks, Luis Moreno, Longcheng Liu,
Batoul Mahmoudzadeh, Pirouz Shahkarami
Royal Institute of Technology, KTH

Olga Maskenskaya, Pär Kinnbom
Svensk Kärnbränslehantering AB

Summary

This feasibility study aimed at investigating if infrared photographs, IR, could be used to locate seepage locations and to estimate the seepage rates. High resolution infrared photographs were used to identify water seepage locations on the walls of an 80 m long drift at Äspö HRL. 166 locations were found over the 220 m^2 large area surveyed. The temperature difference between the moist areas and the dry rock was used to calculate the heat flow used for the evaporation and from this the seepage rate in each spot was determined. The flowrates were so small that in practically all spots all seepage water evaporated. Only a few of these spots could be identified by the naked eye as there was no dripping and the dry and moist rock looked essentially the same. In two of the spots with highest flowrates, water was also collected in paper napkins and weighed. This gave essentially the same flowrates as the IR derived results. Three spots, located in a fractured region, had two to three orders of magnitude lager flowrates than the others, could be identified by their dripping. The seeping water was warmer than the rock surface temperature. Except for these three spots the flowrate distribution can be well described by a log-normal distribution. It was concluded that simple IR photos can be a useful tool to locate where low leakage occurs and that it can be used to estimate seepage flowrates.

Sammanfattning

Denna genomförbarhetsstudie syftade till undersökning om infraröda fotografier, IR, kan användas för att lokalisera var vatten sipprar i sprickor i berg och att uppskatta flödet. Infraröda bilder med hög upplösning användes för att identifiera flödet på väggar i en 80 m lång ort i Äspö laboratoriet. 166 utflödesfläckar lokaliserades över det 220 m^2 stora undersökta området. Temperaturskillnaden mellan de fuktiga och torra områdena användes för att beräkna det värmeflöde som behövs för avdunstningen och därigenom bestämdes flödet i varje fläck. Flödena var så små att det sipprande vattnet avdunstade i praktiskt taget alla fläckar. Endast ett fåtal av dessa fläckar kunde identifieras med blotta ögat, eftersom det inte fanns något dropp och det torra och fuktiga berget såg väsentligen likadant ut. I två av fläckarna med högre flöde samlades också vatten i pappersservetter som vägdes. Detta gav i huvudsak samma flöden som IR-resultaten. Tre fläckar, belägna i ett mer uppsprucket område hade två till tre storleksordningar högre flöden än den andra. Dessa kunde också lokaliseras genom att de droppade. Detta vatten var varmare än bergytans temperatur. Förutom dessa tre fläckar kan flödesfördelningen beskrivas väl med en log-normal fördelning. Resultaten visar att enkla IR-bilder kan vara ett användbart verktyg för att lokalisera var lågt läckage finns och att metoden kan användas för att uppskatta flödena.

Contents

1 Introduction and background 7
1.1 Flow and transport in fractured rocks 7
1.2 Aims and scope 7
1.3 The appendix 8
1.4 The main tool: Infrared pictures to locate leaking spots and estimate evaporation rates 8
1.5 Evaluation of IR information 9
1.5.1 Mass and heat transport during evaporation 9

2 Measurement campaign March 1 and 2, 2016 11
2.1 Description of Äspö HRL and Q-drift 11
2.2 IR equipment 11
2.3 Overview and examples 11
2.3.1 Low flow rates – point seepage 11
2.3.2 High flow rates –point seepage 13
2.3.3 Diffuse seepage 14
2.3.4 Additional examples of IR pictures 15
2.4 Using picture information and supporting measurements 16
2.4.1 General 16
2.4.2 Matching nearby overlapping pictures 17
2.5 Photogrammetry and fracture mapping 18

3 Estimation of seepage rates and channel widths 21
3.1 Determination of seepage rates 21
3.2 An attempt to estimate channels widths 22
3.3 Results 22
3.3.1 Seepage rates from IR and from water collection 22
3.3.2 Channel widths and spot sizes 24
3.3.3 Channel surface density (CSD) 24

4 Uncertainties and possible improvements 25
4.1 General 25
4.2 Uncertainties in evaluating the IR pictures and improvement possibilities 25
4.2.1 Matching different pictures 25
4.2.2 Measuring size of cooled spots 25
4.2.3 Estimating channel widths 26
4.2.4 Energy supply from air and rock 26
4.3 Improvement possibilities 26

5 Conclusions 27

6 References 29

Appendix A Using evaporative cooling to measure flowrates from channels in fractures in rocks 31

1 Introduction and background

1.1 Flow and transport in fractured rocks

Water flow and solute transport in fractured crystalline rocks have gained considerable interest during the last three decades when such rocks were starting to be considered as suitable to host final repositories for high level nuclear waste. This has led to considerable experimental and theoretical investigations of the hydraulic and transport properties at depths down to 1 000 m. An overview of ideas, field and laboratory experiments and model development can be found in Tsang et al. (2015). Conceptualising the rock as a more or less homogeneous porous medium was soon abandoned and it was realised that the presence of fractures with different sizes, transmissivities and frequencies and the presence of zones on different scales needed to be accounted for in the modelling. New approaches needed to be developed to describe the flow and transport processes and new techniques had to be devised to obtain data.

Our concept of flow in fractured crystalline rocks is that preferential flowpaths form in the fractures of the rock and that only a minor fraction of the entire fracture is available to flow. The other parts of the fracture are either closed because the two fracture surfaces are in direct contact or because the aperture is so narrow that only minute flow can pass. Considering that even in fully planar slots between surfaces the flowrate per width[1] of "channel" is proportional to the aperture to the third power, a conduit with an aperture five times less than another conduit will carry 125 times less water per width for a given hydraulic head difference. The channels in one fracture can intersect channels on other fractures at fracture intersections and form complex three-dimensional channel networks. The frequency of conducting channels can be explored by drilling long holes in the rock mass and testing the transmissivity along the borehole. Several techniques exist and are used. The number of transmissive channels per meter borehole and the transmissivity distribution of the channels can be used to construct stochastic conducting channel networks. One common approach is to assume that every transmissive intersection found belongs to a fracture that is fully open over its entire extent. This is the *discrete fracture* model, DFN (Joyce et al. 2010). For this model data of fracture sizes is needed. One drawback of this model is that the assumption of fractures fully open over their entire size obviously is not true.

An alternative approach is to model the network as *a network of channels* that would give the same density of flowing conduits with the same transmissivity distribution if this network were penetrated by boreholes (Gylling et al. 1999). One drawback of this approach is that information of channels widths is needed. This information cannot be obtained by measurements in boreholes with present day techniques. Channel densities can be measured by direct observation on rock walls in underground drifts and tunnels by observing the number of channels per drift wall area (Tsang and Neretnieks 1998). The flowrate distribution of channels can be obtained by collecting the water from each effluent spot. Also channel widths can be measured on rock walls.

1.2 Aims and scope

This feasibility study describes and explores the potential of a novel method to measure the frequency of flowing pathways, here called channels, as well as to assess the flowrate distribution of such channels using infrared photographs, IR, of tunnel surfaces to detect and quantify the seepage rate by the cooling of wet spots by evaporation. The method is limited to so low seepage rates that all emerging water from a channel spreads over the rock surface and evaporates. These low flowrates are expected to be the most frequent for deep geologic repositories in crystalline rocks. Higher flowrates must be determined by other methods.

[1] A channel we visualise as a conduit having a length in the flow direction, an aperture, which is the distance between the two faces of the fracture and a width, which usually much larger than the aperture in the third direction. Both aperture and width can vary along the channel.

The work also aims to define and describe the underlying mass and heat transfer processes on which the evaluation of the IR information relies. A further aim is to try to assess the uncertainties involved in the proposed method.

Being a feasibility study the field-work was limited to one single drift and a few days underground work. The IR based data on flowrates were supplemented by a few measurements by direct water collection for comparison.

A subsidiary but important aim was to show that the IR information can be directly superimposed of visible light photographs used to map fractures in tunnels. The three dimensional map of the tunnel walls can be used to identify fractures from which the seepage comes.

In this, the main report, we emphasize the key ideas, equations and results. The considerable number of detailed equations, their meaning and interactions, derivation and sources are to be found in the appendix. Although all equations are based on long established and well-founded relations the processes are intertwined and the geometries are not always simple, demanding simplifications in order to be computationally manageable. Approximations and assumptions are therefore made. We state, explain and justify these and try to estimate the resulting uncertainties.

1.3 The appendix

Before going to the field the underlying theory and equations to be used for the evaluation were described in detail and anticipated uncertainties were explored and documented. Also some additional ideas on how to supplement and support the IR technique were described and tested in the laboratory. Some of them were later tested in the field and although not all were successful the described ideas are retained in the appendix.

The appendix describes in considerable detail the mass and energy balances and the equations needed to describe heat exchange rates between air water and rock. It also describes in detail how we were to evaluate the IR information. In addition the appendix describes some other ways we intended to test to obtain supplementary information on flowrates. The appendix was a planning document and it was written before the visit to Äspö HRL. It is retained essentially in its original form.

1.4 The main tool: Infrared pictures to locate leaking spots and estimate evaporation rates

Common commercial IR cameras typically have an up to 640×480 pixel resolution and can detect temperature differences down to 0.02 K. For visualisation the pictures can be presented as grey-scale or be given artificial colours e.g. spanning a colour range with red representing warm and blue representing cold with other colours gradually changing in between. The temperature in every pixel is recorded and can be retrieved. The IR camera used has an inbuilt visual light, VL, camera, which simultaneously records a VL picture covering the same area as the IR picture. There are various ways by which to combine the IR and VL information, should that be desired. More advanced cameras exist for military purposes. Software exists by which the data can be processed in different ways.

Figure 1-1 shows a water-conducting channel in a fracture. The channel has a width W. The fracture has only one channel in this case.

Figure 1-2 illustrates the face of a rock surface intersected by a fracture. Seeping water from the fracture spreads over the rock surface by capillary forces and by gravity. When the seepage rate is moderate to low all the seeping water has time to evaporate to the ventilation air. The evaporation energy is taken from the air as well as from the underlying rock. The rock surface is cooled. This is detected by the IR camera, which records the temperature in every pixel.

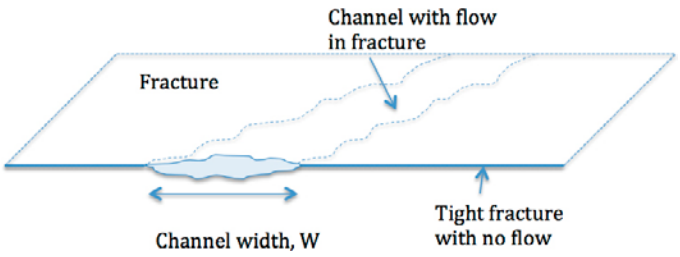

Figure 1-1. *A water-conducting channel in a fracture. The channel has a width W where it intersects the drift.*

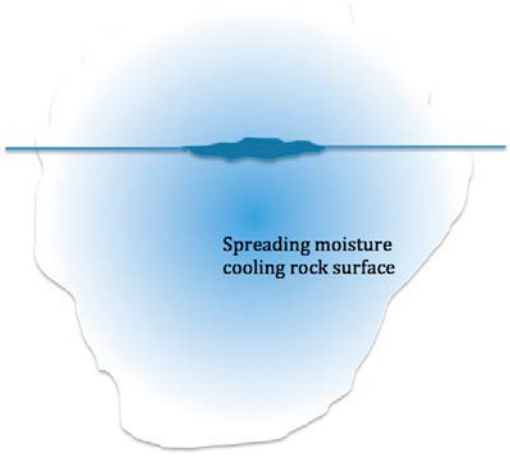

Figure 1-2. *Seeping water in the fracture spreads over the rock surface by capillary forces and by gravity. The evaporation energy is taken from the air and from the underlying rock. The rock surface is cooled.*

1.5 Evaluation of IR information

1.5.1 Mass and heat transport during evaporation

Water that emerges from a channel in the rock spreads on the surface to the surrounding drier areas. When the air in the tunnel or drift has a lower relative humidity, RH, than that of the water film where RH = 1, this evaporates, cooling the water and the underlying rock. The temperature is recorded by the IR picture and can be used to derive the evaporation rate and thus the seepage rate from the channel. For his calculation information is needed on the heat transfer coefficient between air and water film and of the heat flux from/to the rock. The heat transfer coefficient for forced convection can be determined from information of the ventilation air velocity and tunnel dimensions. In addition the temperature and RH difference between water film and air generates air flow by the density difference of the air nearest the film and the bulk air. This free convection generates additional heat transfer. The heat transfer rate from the rock can be assessed from information on interior rock temperature and dry surface rock temperature. These processes are described in detail in the appendix and summarised in Chapter 3.

When seepage rates are larger than what can be carried away by evaporation of the wet film, streams of water form either as falling streams on the surface or as dripping or flowing streams. The falling stream can be collected by soaking a cloth or “diaper” and weighing. Dripping water can be collected in a beaker. In the type of low permeability rocks considered for a repository the larger flowrates are not expected to be very common. This is supported by the present tests. See Chapter 3.

2 Measurement campaign March 1 and 2, 2016

2.1 Description of Äspö HRL and Q-drift

The nearly 80 m Q-drift at a depth of 450 m below the surface was photographed on both sides. The ceiling had been covered by shotcrete and was not photographed. The drift was first supplied with markers that were accurately triangulated. Hand warmed magnets were placed adjacent to the markers. These warmed magnets showed up clearly on the IR photos and were used as an aid to align IR photos onto tunnel topography. The drift had previously been photographed with a high-resolution wide-angle lens (90-degree) VL camera. This was used to supply the information used for generating the 3D visualisation of the drift and can be used to accurately map fractures in the Rock Characterisation System, RoCs (SKB 2014). Considerably more IR than VL photos were needed because of the narrower angle of the IR camera, which, however also supplied its own VL pictures covering the same area as that IR picture. This was helpful for locating the exact location in the 3D-tunnel where the cool spots could be overlain. This process was done manually in this first testing but is possible to automate more if more markers are allocated on the rock walls.

2.2 IR equipment

The camera used was a FLIR 650sc with a 640 × 480 pixel resolution for IR pictures and a temperature resolution of 0.02 K. It was fitted with a 45-degree lens for the widest frame size 640 pixels. The temperature accuracy for ambient temperature is ± 1K. The pictures can be analysed with the software FLIR Tools. This allows measuring mean, minimum and maximum temperatures in arbitrary size circular or rectangular regions, lines, and in any point in the frame. Many different colour schemes can be selected for visualisation. The temperature range to be spanned over the entire frame can be selected allowing bringing out locations on the frame with a narrow temperature difference. In practice spots with temperatures between t_{min} and t_{min} + 0.1 K or even better can be visualised. This technique was used to try to estimate channels widths and effluent point sizes.

2.3 Overview and examples

In this section we present some IR and VL pictures and show examples of how the information was used. Some uncertainties in using the information are exemplified in order to demonstrate that there are some subjective choices that influence the quantification of the flowrate determination and width. In all, 166 cool spots were found in a 60 m long section in the 5 m high drift. Both the left and the right sides of the drift were photographed. All this covers an area of about 220 m^2. Some areas were not visible behind equipment and some areas had been subjected to dense slit sawing and were not included where obviously this has disturbed the cooling pattern.

We show examples of low flow rates – point seepage, high flow rates – point seepage as well as diffuse seepage.

2.3.1 Low flow rates – point seepage

Figure 2-1 shows an IR picture of a vertical wall section in a drift that was excavated by blasting about 15 years ago (Magnor 2004). The picture shows a section about 4 m wide and 3 m high. The temperature scale on the right hand has been set to span the region 8.5 to 12.5 °C. Figure 2-2 shows nearly the same area taken by a normal camera sensitive to visual light, VL. In this location thin streams of water could be seen by the eye emerging from the two spots that can be identified at the apexes of the blue region. In the VL picture it is seen that in the cool region the rock is tainted light brownish. This is probably ferric iron oxide and that has precipitated from the effluent water as it emerges into the drift, meets oxygen that oxidised dissolved ferrous iron, which precipitated as “rust”.

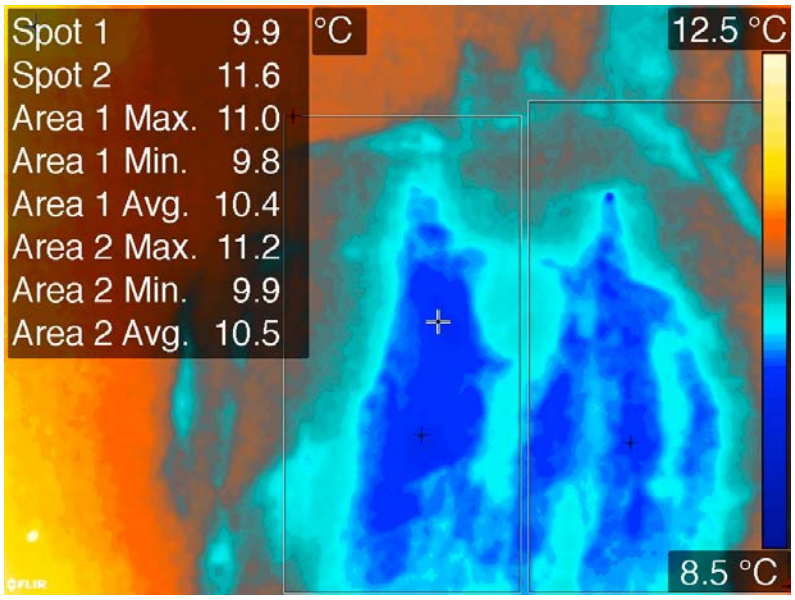

Figure 2-1. *Picture #1913, Location 70Lb.*

Figure 2-2. *Picture #1914, Location 70Lb.*

The information underlying the IR picture can be used to measure temperature in each pixel and to supply information of mean temperature in circular or rectangular areas. Two of the latter are shown in the picture. From the information in the picture the temperature difference between "dry" rock surfaces and surfaces on which there is a seeping water film can be obtained and the size of the cooling area can be assessed. This information is then used to determine the evaporation rate. This is equal to the seepage rate of water from the channel(s) if no water reaches the floor of the drift. In this case practically all water evaporated, although some reached the region in the picture (not shown) below that in Figure 2-1 (*Location 70La)*. The width of the channel(s) can be estimated from the size of the effluent spot. In this case there are two effluent points (channels), which are about 2 and 5 cm wide.

In this location the water was actually seen to be seeping. It was collected by soaking it in paper napkins and measuring the effluent rates. They were 54 and 76 g/hr. This is valuable information because it can be used to compare to the seeping rates determined by using the temperature information

in the picture. We pre-empt those results by stating that this gave 36 and 52 g/hr from the IR data. Considering the many uncertainties involved we deem this to be acceptable agreement for the present purposes. That will be discussed later. The VL picture shows the same area as Figure 2-1 does.

2.3.2 High flow rates –point seepage

In two fractured zones the flowrates in three spots were some orders of magnitude larger and the streaming water was at least a degree warmer than the "dry" rock. This suggests that this water comes from regions in the rock further away from the surface of the drift where the rock temperature is not influenced by the ventilation air. This water flows so rapidly that it is not cooled appreciably by the cooler rock it the water approaches the drifts surface. This suggests that the channels are very narrow because wide channels have a large flow wetted surface that facilitates for the water to continuously adjust to the local rock temperature along the flowpath.

IR and VL pictures of the warm effluent are shown in Figures 2-3 and 2-4. It may also be noted that also this effluent channel is only cm's wide and lies at the border of a warmer and cooler rock region.

The flowrate of "hot" water was measured by collecting and weighing it to be 14 500 g/hr from the upper spot. This is several orders of magnitude larger than from the cold spots in Figure 2-1.

The VL pictures in Figure 2-4 show that the zone, the brownish area becomes wider lower down. The right hand IR picture in Figure 2-3 shows that there is an additional warm effluent a bit lower down in the "falling" warm stream. Also this is a narrow, a few cm wide, effluent.

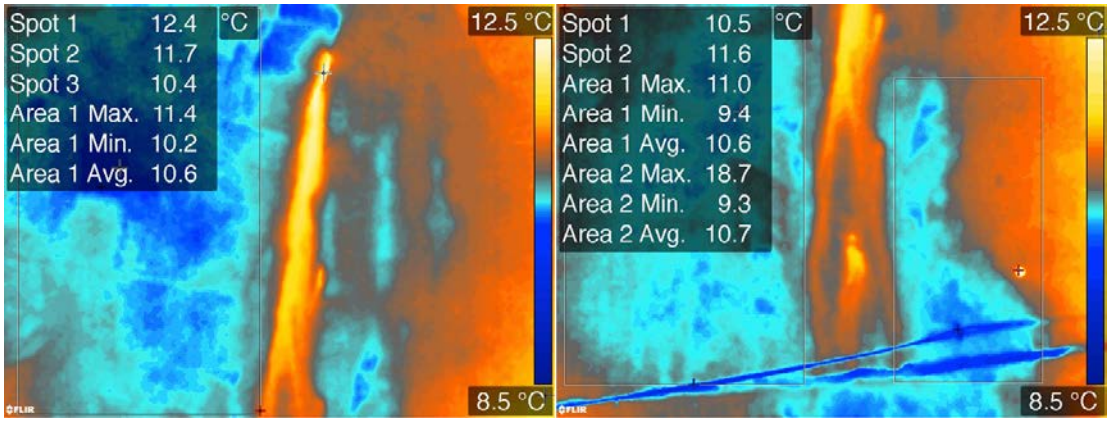

Figure 2-3. *Picture #1919, Location 64Lb lies partly above #1917, Location 64La.*

Figure 2-4. *Picture #1920 (left), Location 64Lb lies partly above #1918 (right), Location 64La.*

2.3.3 Diffuse seepage

Another example is shown in Figure 2-5 where there seems to be a larger region for the water effluent area. Below we show that by displaying the temperature in a narrower range it is possible to obtain an impression the size of the effluent channel(s).

In Figure 2-5 the effluent location seems to cover a large region as if the rock were a porous medium allowing the water to seep out over a large area. The seepage seems to be high in the centre of the wetted spot and then falls off toward the edges. In our opinion this is not the case. The water seeps out in a narrow part of a fracture (channel) but the flowrate is so small that gravity does not cause it to flow down the vertical wall more rapidly than the water spreads by "capillary" wetting of the surface of the rock face. As it spreads it is gradually cooled less as can be seen in the left picture. The size of original effluent spot cannot be determined from the IR picture. However it is illustrated in the right hand picture that by narrowing the temperature region to 0.4 °C the spot shrinks considerably. Narrowing down the temperature range even more does little to the size and the shape of the spot. The resolution of the IR camera is 0.02 °C. We tried to use this way of narrowing down the temperature range to estimate an upper bound of the effluent size, admitting that this gives crude estimates. This often gives spot sizes of ten to a few tens of cm although larger values have been found.

It should be noted that the size of spots visualized in this manner may not be directly correlated to the width of the channel and may not even exactly show its location because the seeping water is expected to have a somewhat higher temperature, as it emerges from the interior warmer rock, than that of the film surface as the water first has to spread and be cooled.

Another example is shown in Figure 2-6 where spots are about 10 cm wide.

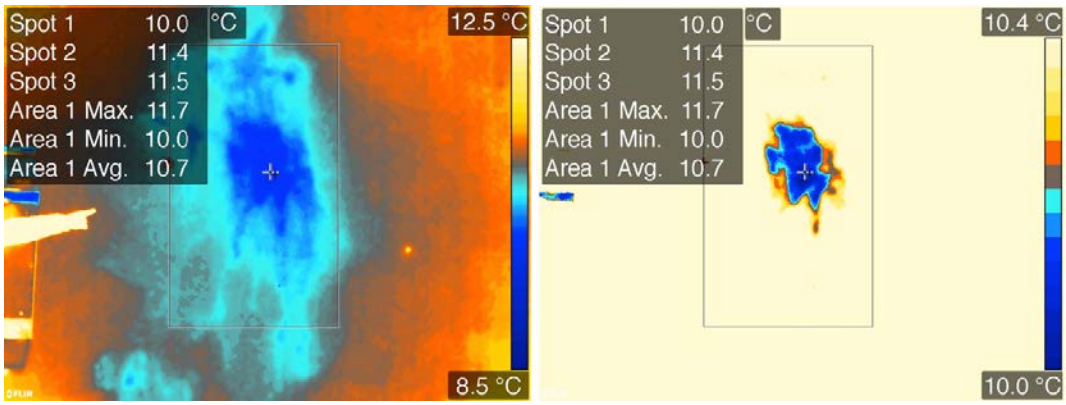

Figure 2-5. *#1895, Location 20Lb. Same picture in two different temperature scales.*

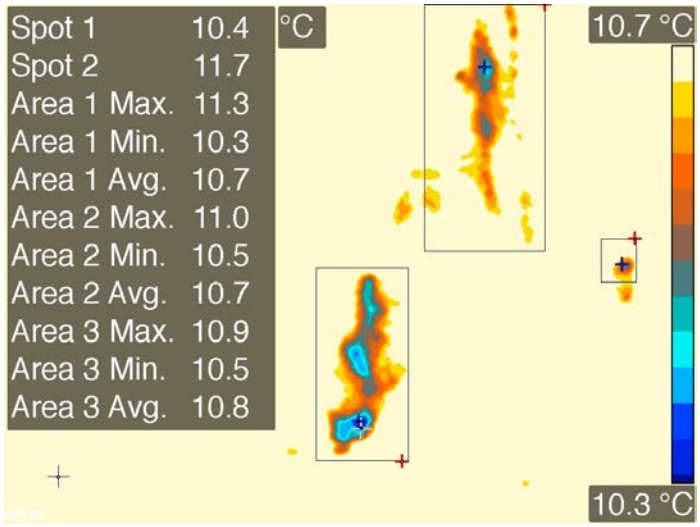

Figure 2-6. *#2079, Location 23Ra. An example of what seems to be narrow spots.*

2.3.4 Additional examples of IR pictures

Figure 2-7 shows the temperature around and inside a shallow nearly horizontal air-filled borehole. It illustrates that a short distance into the rock the temperature is considerably higher, 12 °C, than on the warmest location on the surface of the rock 11.5 °C that could be taken for "dry" rock temperature.

Figure 2-8 shows the same area displayed in the two different temperature ranges. This is another illustration of the small size of effluent points. It illustrates the difficulties of determining the actual width of a channel. Supplementary methods must be developed.

Figure 2-9 shows an example where a "hot" fluid 13.4 °C emerges close to other spots with low seepage rates that allow the fluid to spread by surface migration and be cooled by evaporation. The flowrate of the "hot" fluid is about three to four orders of magnitude larger than in the other spots and the fluid runs rapidly down the rock wall. It could be collected and its flowrate was measured to be 17 500 g/hr. The other spots had flowrates up to 160 g/hr. There is no obvious visible indication that the rock near the "hot" spot is markedly different from the surrounding rock.

Figure 2-10 shows the region just below that in Figure 2-9 in IR as well as VL. In the VL picture it is seen that a brownish coating generated by precipitation of ferric ion and microorganisms has stained the rock.

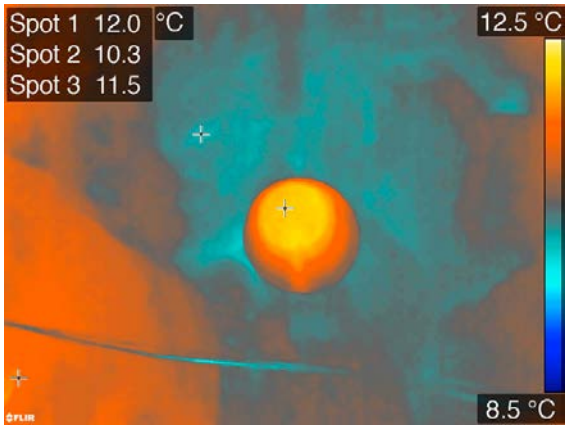

Figure 2-7. *#2097, Location 56La. Temperature around and in a borehole with diameter 31 cm and depth 165 cm.*

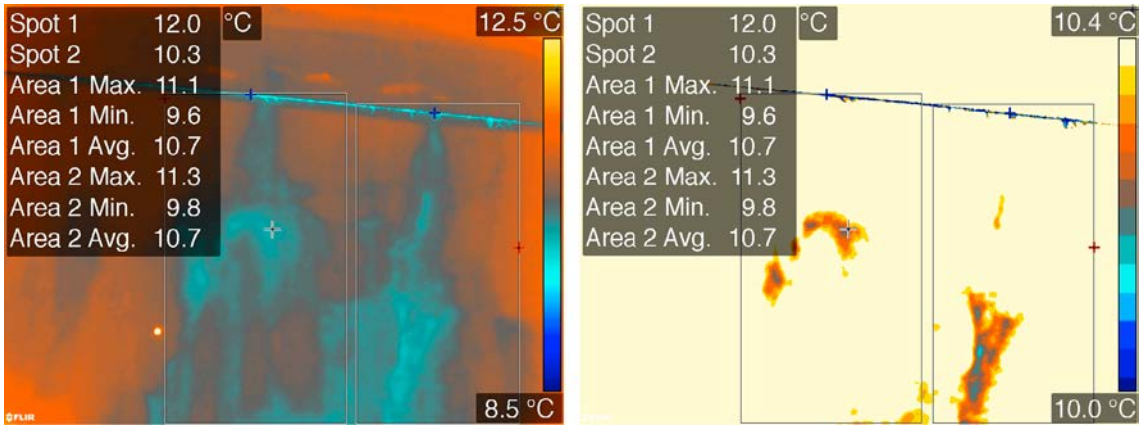

Figure 2-8. *#2065, Location 33Rb. The same area shown in the two different temperature ranges.*

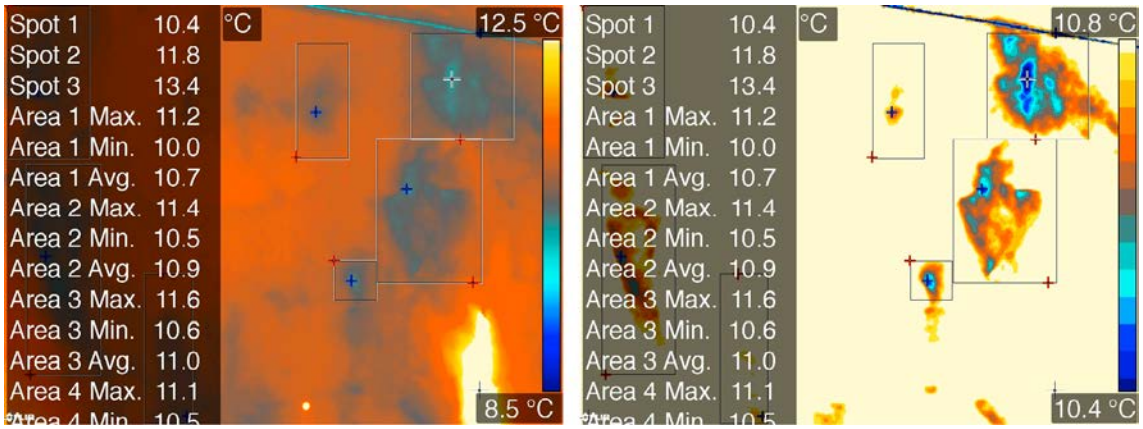

Figure 2-9. *#2057, Location 38Rb. The same area shown in the two different temperature ranges. Note the effluent of "hot" fluid. 13.4 °C, in the lower right hand corner*

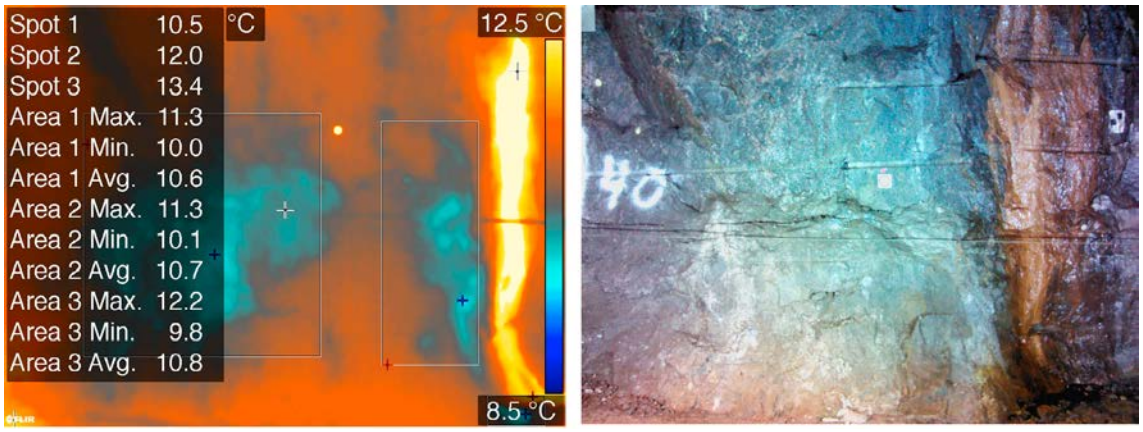

Figure 2-10. *#2055 and #2056, Location 38Ra. Region just below that in Figure 2-9.*

2.4 Using picture information and supporting measurements

2.4.1 General

The IR camera sets the colour scale automatically to span the whole range of temperatures in the area covered by the photograph. In the drift the range typically was from about 8 to 14 °C or higher if e.g. a hand of person was in the frame. One can choose different colour schemes. We use "Arctic", which displays the warm regions as red to white with increasing whiteness for higher temperatures and blue for the cold regions. This is shown on the right vertical ribbon on the pictures.

After some testing the temperature range in all pictures was adjusted to lie between 8.5 to 12.5 °C for visualisation purposes. This covers the temperature range of most of the "dry" rock areas as well as those where evaporative cooling takes place. The air temperature is measured by thermometers and is also determined by measurements on different pieces of installed equipment that are exposed to air flow on both sides and thus do not obtain heat by conduction from the rock. The air temperature varies very little along the drift. Air relative humidity was measured to be typically around 50%. Air velocity was determined by anemometer measurements at the exit of the two air ducts at the end of the drift where air velocity was high enough to be measured. From this information the mean air velocity in the drift was found to be 0.2 m/s. This is the lowest velocity the anemometer can measure and as it then behaved erratically the air velocity throughout the drift was taken be 0.2 m/s. This low velocity adds little to the convective heat transfer coefficient, which is dominated by that due to natural convection caused by the temperature and RH differences between the air close to the wet

evaporating regions and the bulk air. As also discussed later the heat used for evaporation is mostly supplied by conduction from the rock. The heat supplied by heat transfer from the air is a minor fraction of the total heat supplied for evaporation.

2.4.2 Matching nearby overlapping pictures

Commonly three picture pairs were taken from the same location using a tripod. In most places the tripod could be set with the camera at a distance of about 4 m from the opposing wall. In some location fenced off sections allowed only a shorter distance between camera and opposing wall. One picture was taken pointing horizontally. This covered a region from and including a small section of floor and about 2–2.5 m above. For the next picture the camera pointed about 30-degrees upward and it was attempted to include some recognisable feature in both the earlier picture as in the 30-degree picture. A third picture pointed even higher to include the rest of the wall and the ventilation duct near the ceiling. Similarly it was attempted to obtain overlaps to the left and right when moving the tripod about 3 m. Each picture typically covers 4 metres horizontally.

In the subsequent matching of pictures up/down and sideways it was found that the IR visible cool spots could look different in matching pictures. This is illustrated in Figure 2-11. The three pictures stacked above each other display an about 4 m wide and 5 m high section of the tunnel wall. The lowest starts at the floor, the highest includes the ventilation duct near the ceiling. The middle picture overlaps the other two.

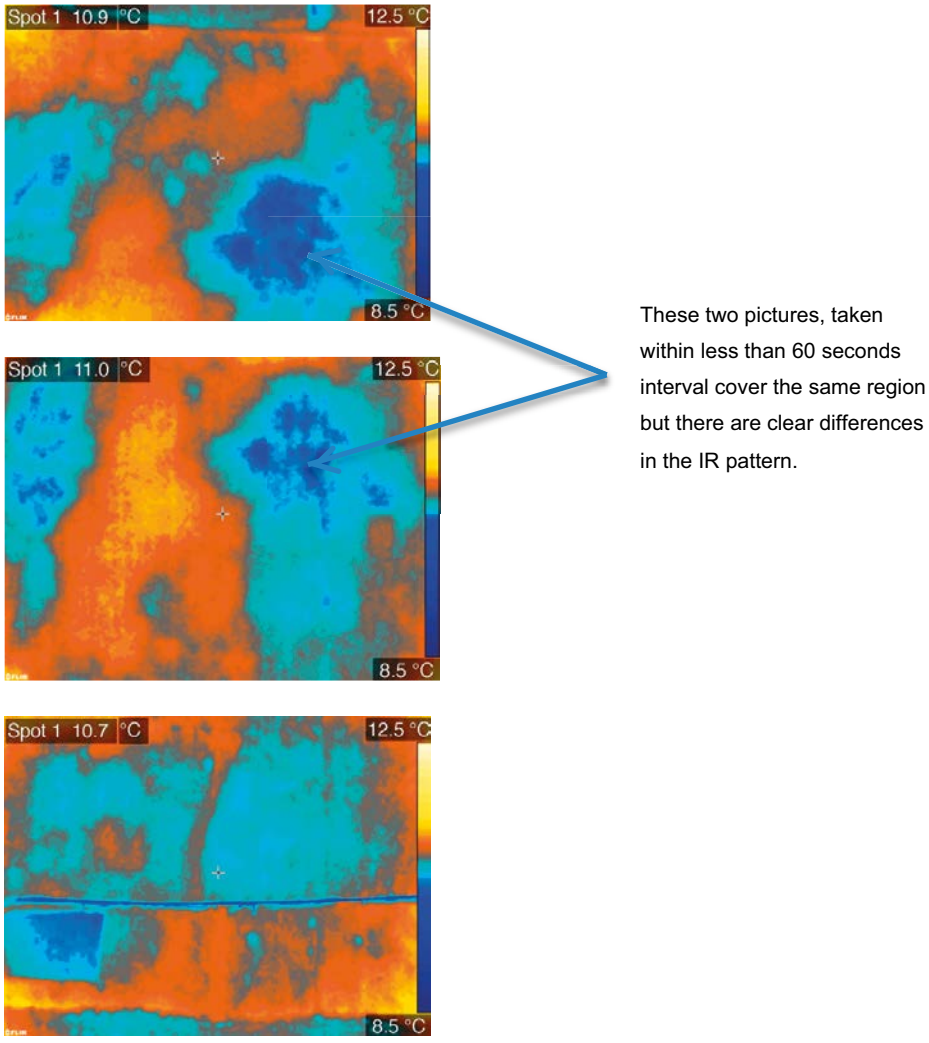

Figure 2-11. *#2109, 2111 and 2113 from bottom and up, Location 62La, b and c. The three pictures show a section of rock wall from floor to ceiling. The lower and upper pictures overlap the middle by about 30 %.*

2.5 Photogrammetry and fracture mapping

A 3D tunnel model was created using a ShapemetriX3D system for generating a three dimenitional, 3D, images and their assessment. That was achieved by obtaining a number of pairs of digital pictures (stereoscopic image pairs) of the tunnel surface. Two pictures were taken from different positions ensuring that each pair shows the same rock surface. 3D images were generated from the stereoscopic image pairs, and then were merged onto a final 3D tunnel model. That resulted in acquiring of tunnel relief and its texture. This 3D model geometry and texture was used as a base for creating an IR model.

The IR pictures were accurately aligned onto VL photos taken by the infrared camera, and then onto photos taken by ShapemetriX3D camera. The work was done manually, using Photoshop software. The hand-warmed magnets and other elements observed on a tunnel surface served as an aid for the manual photo alignment. IR pictures were stitched together creating a digital canvas that was used as texture, and then applied onto 3D tunnel relief. The resulting infrared 3D model of the tunnel could be combined and visualised with RoCS mapping data in such way that IR texture and mapping data assigned to the real-world coordinates by dereferencing.

The photogrammetry is a method of creating a 3D model of a tunnel based on a stereoscopic principle. The model was computed from a pair of digital photos for each area of interest that were acquired by standard digital camera. The model consists of texture, i.e. visual light pictures of the tunnel surface, and a 3D tunnel surface topography. This 3D model was a foundation for creating a 3D infrared model. Infrared model was computed by the replacement of visual light photos with the infrared photos and accurate aligning them onto 3D tunnel topography.

Geological data could be acquired in Rock Characterization System, RoCS, which is the part of SKB's tools for geological data management and visualization (SKB 2014). RoCS allows accurate tunnel mapping using 3D tunnel model and the coordinate measurements of the reference points. The mapping data consists of geo-referenced objects and a set of their attributes. Data acquired by RoCS, including fractures and fracture zones, can be aligned onto 3D infrared tunnel model in order to link water-bearing zones with the mapped fracture network. The individual visible light pictures for the stereoscopic continuous view of the drift are stitched together into one large file. The file is coupled to the coordinate system in a way that makes it possible to accurately locate any point on the surface of the drift. It is possible to couple mapping information, i.e. location of fractures and rock types, to this file in RVS-software. The IR photographs are arranged in another layer that can accurately be superimposed on the former layer. This makes it possible to identify in which fracture and rock type the seeping water identified by IR is located. The view of the drift can be moved, turned and rotated in three dimensions. It is possible "walk" along the drift and "look" at the walls with the proper software.

Figure 2-12 shows an IR picture of the entire drift. The colours indicate temperature with red the warmest and blue the coldest. The temperature contrast is not to scale and exaggerated for visualisation purposes.

Figure 2-13 shows a section in the drift looking into it.

Figure 2-14 shows an IR view of a small section, 52–60 m, of the wall on the left hand side. The stitching in this case is not as seamless as the visible light pictures in these first exploratory tests. They had to be made manually in this case because the visible light pictures were obtained originally with a different purpose and were not automatically coordinated with the IR pictures taken much later. It is nevertheless possible to identify in which fracture(s) and rock type the seeping water is located. For detailed analysis one can refer to the original IR pictures.

Several ways of improving and facilitating the work have been identified. The IR camera has an inbuilt visible light, VL, camera that simultaneously records VL together with IR. The VL lens has a similar focal length but it has not yet been tested if it has a resolution and other properties that fulfil the need for stereographic mapping of the fractures. Alternatively using a VL lens with the same focal length as the IR and mounted on the same tripod, the pictures will be automatically well aligned. If the technique is to be frequently used it is worth the effort to pre-program the lens-correction parameters so the unavoidable distortion difference between the two different lenses is minimized. The work-flow could be considerably improved if VL and IR pictures can be pixel-to-pixel aligned when taking the pictures. This would avoid manual adjustment afterwards.

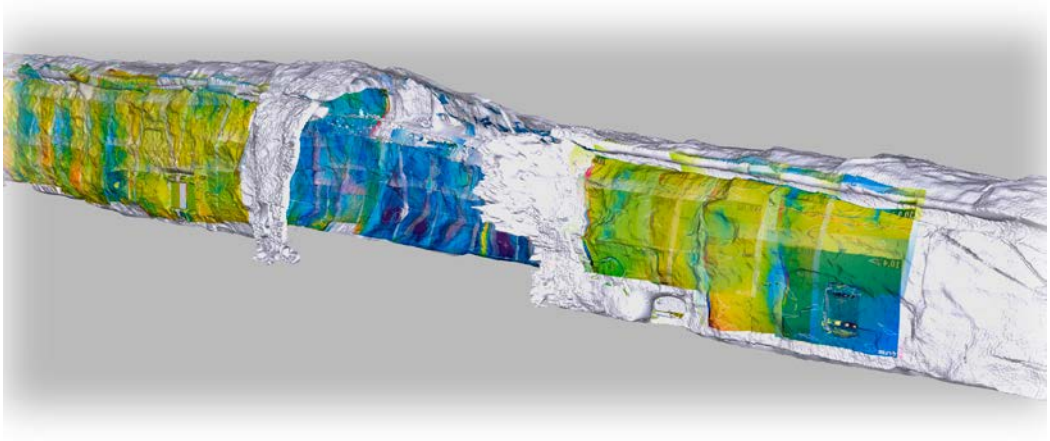

Figure 2-12. *The drift seen in one perspective, the entrance is on the right. The "open" part in the middle is a region with different equipment and installations are hiding the wall.*

Figure 2-13. *View into the drift. Left frame shows the IR layer and right frame the visible light layer.*

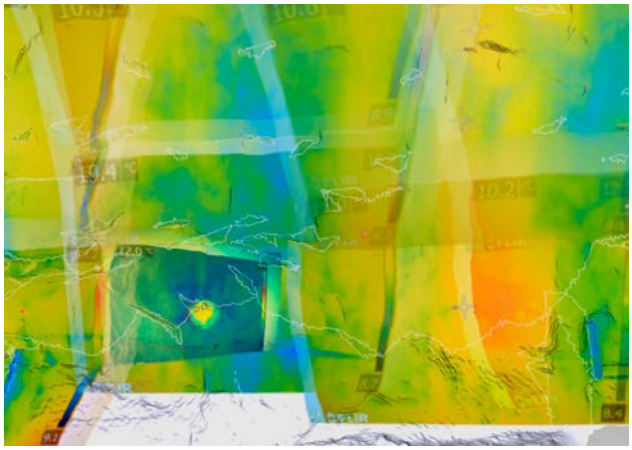

Figure 2-14. *IR view of a small section, 52–60 m, of the wall on the left hand side of the drift.*

The Colour scheme to visualize temperature is artificial and can be selected by the operator. In automatic mode the software sets a "reasonable range to display for every picture. Every picture can have a different span. The IR cameras temperature scale settings, which were set to automatic, can be set to a given temperature span to avoid "jumps" in temperature when stitching nearby pictures. The above actions will considerably facilitate the handling of the multitude of pictures.

3 Estimation of seepage rates and channel widths

3.1 Determination of seepage rates

We present only the central formulas used here. More detailed descriptions can be found in the appendix.

Knowing the heat of evaporation the seepage rate m_{evap} [g/s] is obtained from the evaporation energy per second Q_{evap} [W] knowing the heat of evaporation ΔH_w [J/g]

$$m_{evap} = Q_{evap}/\Delta H_w \tag{3-1}$$

where

$$Q_{evap} = Q_a + Q_r \tag{3-2}$$

Q_{evap} is the energy used for evaporation, Q_a, coming from the air and Q_r from the rock. These in turn are obtained from information on the temperature difference between the air and cooling water film $T_a - T_f$, the size (width and the height) of the cooling area A_{spot} and the heat transfer coefficient h_a. The latter depends on the ventilation air velocity and tunnel dimensions and on the vertical air velocity component induced by the cooling itself.

$$Q_a = h_a A_{spot}(T_a - T_f) \tag{3-3}$$

The heat transfer coefficient for forced convection $h_{a,forced}$ is about 0.8 W/m^2/K at the measured air velocity 0.2 m/s in which case the flow is turbulent. Also the heat transfer coefficient for free convection on a vertical surface with a height of $H_{spot} \times h_{a,free}$ can be derived from Bird et al. (2002) to be

$$h_{a,free} = 1.5 \sqrt[4]{\frac{(T_a - T_f)}{H_{spot}}} \text{ W/m}^2\text{/K} \tag{3-4}$$

The combined heat transfer coefficient h_a is taken to be

$$h_a = h_{a,free} + h_{a,forced} \tag{3-5}$$

The heat from the rock is estimated by

$$Q_r = -\lambda_r A_{spot} \left.\frac{dT}{dx}\right|_{x=o} \tag{3-6}$$

where λ_r is the heat conductivity of the rock, about 3 W/m/K and $\left.\frac{dT}{dx}\right|_{x=o}$ is the temperature gradient in the rock at the surface of the rock. The latter is determined by solving the equation describing the heat transport in the rock i.e. Fourier's law. Simplifying assumptions on the geometry of the heat transfer need to be used because of the complex form of the cooling area and underlying rock. The heat conducted from the far away rock and from the regions surrounding the cooled spot is idealised to come with spherical symmetry. Then a very simple expression can be derived to assess Q_r namely

$$Q_r \approx \sqrt{2}\pi r_{spot}(T_r - T_f) \tag{3-7}$$

r_{spot} is the radius of an area equal to the cooled area in the IR photograph. It is approximated by (Neretnieks et al. 2010, Section 5.4).

$$r_{spot} \approx \sqrt{\frac{W_{spot} H_{spot}}{\pi}} \tag{3-8}$$

when measured as a rectangle with width W_{spot} and height H_{spot} or by some other suitable means if the spots are very irregular.

A test was made comparing the seepage rate results using the above approach with that obtained by actually collecting the seeping water by soaking it in napkins and weighing. The differences were deemed to acceptable, considering the uncertainties involved. This will be discussed more in the results and discussion sections. It is acknowledged that there are considerable uncertainties in the above simple equations. Uncertainties will be discussed in a later section.

Seepage rates were measured in five locations where seepage could be seen by the naked eye and where the seepage was identified to come from a small spot. This was done by holding paper napkins and/or towels over the spot until sufficient amounts of water had been collected. The water mass was determined by weighing.

Another method was also tested. A small amount of fluorescent dye was injected just below the effluent point. The falling rate of the fluorescing dye was observed in ultraviolet light by intermittent photographs and by producing movies. These attempts were not successful because the fluorescence was not intensive enough for the movies and because in the high flow areas where this method was expected to be most suited often minor drops of dyed water were released and fell down some distance interfering with the more even flow of the film. More development is needed if the technique is to be useful.

3.2 An attempt to estimate channels widths

An attempt was made to estimate channels widths from the IR pictures by first limiting the temperature range in the pictures to the span of the temperature of the spot +0.4 °C as in Figures 2-6, 2-8 and 2-9. Spots that lay approximately on a line and closer to another spot than 0.5 m were taken to belong to the same channel and its length was set by the distance from the outermost spots on the line. This is illustrated in Figures 2-6 and 2-8. The size of the spot was measured in the darkest region. The rationale for this is that when the water from the channel emerges it immediately starts to spread out over the rocks surface whereby it starts to cool by evaporation. It was found that there are some subjective choices in this procedure. The choice of the temperature span is one. Several spans were tested. A too narrow temperature range, 0.1 °C, made some spots disappear. A larger spread seemed to increase the spot size by a factor of two or more. This is one of the weak points in the procedure and it seems to result in too wide channels. Another weakness is that when there seemed to be several adjacent areas with cool spots in more than one location from which less cool areas spread it was not obvious if these were individual effluent spots of if the minor temperature differences were caused by slightly different evaporation rates. The latter cause is quite credible considering that the drift was blasted. The uneven surface is likely to have different local evaporation rates between nearby “hollow” and “protruding” locations. Different attempts to assess spot widths could give very different results and this approach was deemed not to give reliable results. The five high flow spots from which water was physically collected by soaking in napkins and towels all had widths less than 10 cm. Earlier observations of precipitation curtains in tunnels in crystalline rocks suggest that channels widths seldom are larger than some tens of cm. Very narrow channels are often observed at fracture intersections, (Tsang and Neretnieks 1998).

3.3 Results

3.3.1 Seepage rates from IR and from water collection

Seepage rates from 166 spots are shown in Figures 3-1 and 3-2. Note the logarithmic scale. In all of these spots except the three “warm spots” with visible dripping all the emerging water spread over an area sufficient to evaporate all seepage. Two of these spots, i.e. #1 and #2 in Table 3-1, were also measured by collecting the water in napkins. Table 3-1 compares the results. The table also gives information on the three additional spots with very high flowrates. These had several orders of magnitude higher flowrates than all the other spots and the seeping water was much warmer that even the high temperature regions on the “dry” areas. This is clearly seen in the IR photographs referred to in the table. It is also noteworthy that the widths of high flow spots are readily observable on the photographs and are very narrow. Four of the five mentioned spots are 5 cm or less wide. The fifth is estimated to be about 10 cm wide.

Figure 3-1 shows a histogram of channel flowrates when the dry rock temperature T_r is set to 12 °C for all spots. Note that it displays the logarithm of the flowrate. The distribution resembles a lognormal distribution except for the three outliers.

The mean and standard deviation of the logarithm of the flowrates are 1.5 and 0.53 respectively.

Similar to Figure 3-1, Figure 3-2 shows the observed flowrate distribution when the rock temperature for each channel is taken to be the highest temperature seen in the picture where the spot was found. The mean and standard deviation of the logarithm of the flowrates are 1.4 and 0.55 respectively. The difference between the diagrams is not large. This suggests that the results are not very sensitive to how the dry rock temperature was chosen. Both diagrams include the three "hot" flowrates that have more than two orders of magnitude larger flowrates than the mean of those in the histogram. It looks as if the channels with the high flowrates belong to another distribution. These spots were located in an area with more intensive fracturing.

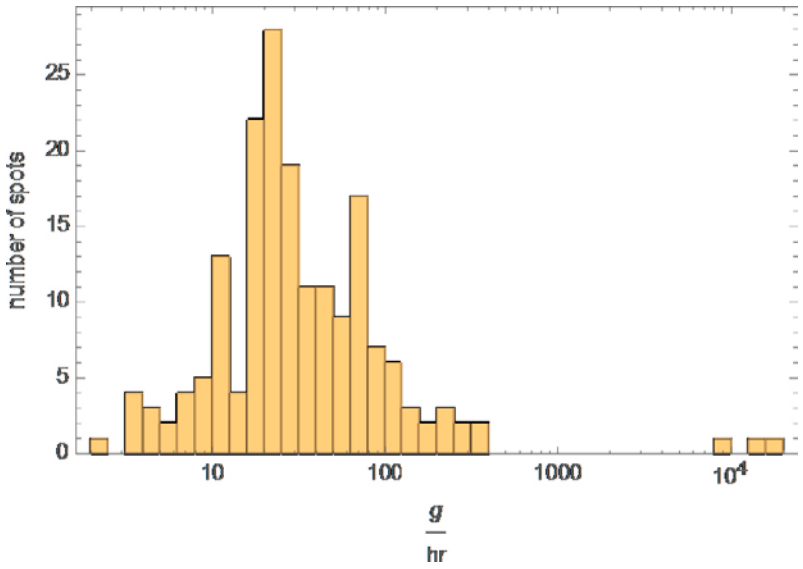

Figure 3-1. *Histogram of channel flowrates when the rock temperature T_r is set to 12 °C for all spots. (program: histogram data Äspö II. nb).*

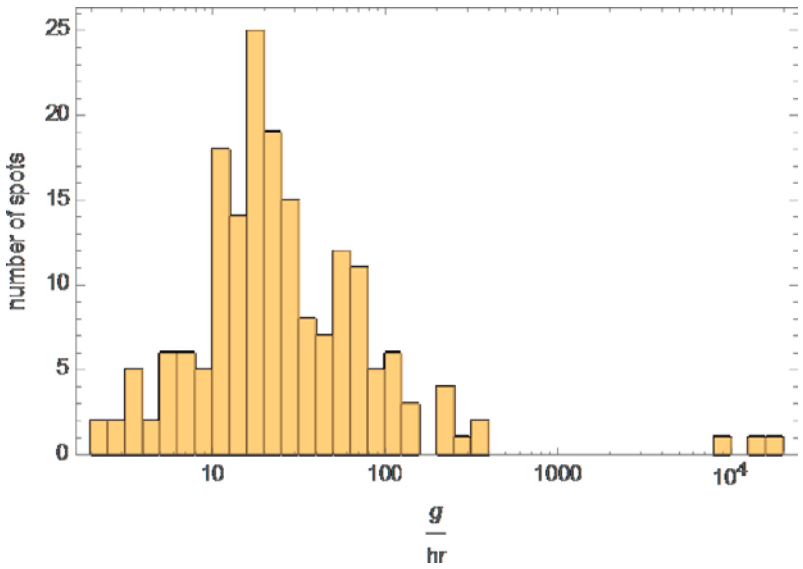

Figure 3-2. *Histogram of the flowrates when T_r is set to the largest value found in the picture in which the spot was found for all spots. (program: histogram data Äspö II. nb).*

3.3.2 Channel widths and spot sizes

These channel widths were estimated by visual inspection of the pictures.

Table 3-1. Seepage in g/hr in spots measured by IR and by collecting and weighing.

Spot #	From IR	By weight, g	Channel width, m	Comment
1	36	54	0.05	Figure 2-1
2	52	72	0.07	Figure 2-1
3	–	14 500	0.05	Warm effluent Figure 2-3 and 2-4
4	–	8 300	0.05	Warm effluent Figure 2-3 and 2-4
5	–	17 500	0.1	Warm effluent Figure 2-9 and 2-10

Figure 3-3 shows a histogram of sizes of the cooling area estimated from the rectangles used to estimate the spot sizes in the figures. The mean and standard deviation of the size is 1.0 and 0.78 m respectively. The channels widths are considerably smaller as discussed in Section 3.2. The attempts to estimate channel widths by narrowing down the temperature difference around the effluent spot suggest that the width is mostly less than 10 cm. New method(s) must be devised to determine the widths of the channels in the spots that are detected by the IR photos.

3.3.3 Channel surface density (CSD)

In channel network models the size (length and width) and density of channels is important. This has been discussed in Neretnieks (2017). A measure of the density is the channel surface density. CSD, which is a measure of how many channels per area will intersect a given plane cutting through the rock. The CSD is estimated to be the 166 channels intersected by the 220 m^2 surveyed area of the Q-drift. CSD = 0.75 channels/m^2. This is much larger than found by other techniques that cannot detect low flow seepage channels (Neretnieks 2017). This suggests that a large fraction of fractures have one or more fractures.

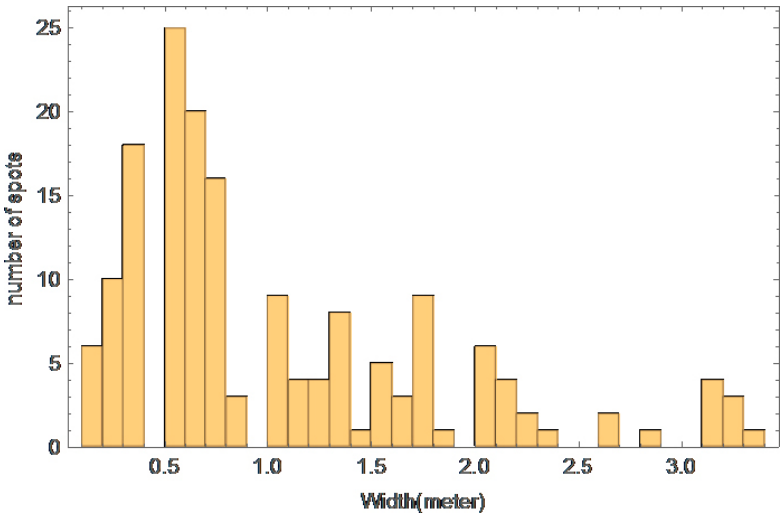

Figure 3-3. *Histogram of the spot sizes. (program: histogram data Äspö II. nb).*

4 Uncertainties and possible improvements

4.1 General

The uncertainties in the seepage data from IR can be assessed by measurements with other techniques of each spot found by the IR pictures. The “diaper” method seems to be a reliable method, facilitated by the knowledge gained from IR pictures of where to apply the diapers.

The mass and energy balance approach is based on fundamental laws of physics. The correlating equations in the appendix of heat and mass transfer between rock, water film and air are well established. However, the geometries underlying of heat transfer radially, axially and tangentially are by necessity considerably simplified to allow using analytical expressions and because of lack of information of where the channels deeper inside the rock are located.

4.2 Uncertainties in evaluating the IR pictures and improvement possibilities

4.2.1 Matching different pictures

It was sometimes not obvious how to superimpose the pictures even though a detailed protocol had been made for each picture. This was mostly because two adjacent pictures showed the temperature pattern differently. This is illustrated in Figure 2-11. There are several causes for such differences. The IR camera records the IR light intensity that reaches its sensor. This light intensity depends primarily on the temperature of the source and by the emissivity of the material. In the present case it is the crystalline rock, mostly Äspö diorite. Crystalline rock covered by a water film that can have variable thickness. Both rock and water have an emissivity[2] of 0.95 (FLIR). However, the emission intensity varies with the angle perpendicular to the emission surface. The surface of the blasted rock is not even. This can cause different emission patterns when the camera is moved. The temperature difference between darkest blue and the somewhat lighter blue in the picture is about 0.1 °C. Other potential sources of error are that the presence of other heat sources may radiate heat to the rock wall in the picture. This heat can be partly reflected back from the wall to the camera. There were four persons moving around, one behind the camera and the other three often near but just outside the picture, tending to different tasks. Their movement also potentially could influence the air movement and thus indirectly influence the evaporation rate and thus the temperature of the cooling spots.

In some areas the wet rock surface had a film of wet “slime”, probably a mixture of microorganism and ferric iron precipitates, the brownish colour in Figure 2-4, which may have a different emissivity than water and rock. Another reason for local differences may be that the mass and heat transfer coefficient varies due to the uneven surface topology. Local deeper lying sections may not be exposed to the airflow in the same way as asperities.

One of the difficulties in matching the pictures was that the IR camera had a maximum 45-degree lens. The camera used for the photogrammetry pictures had a 90-degree wide-angle lens for the RoCs system. The identification points on the wall of the drift were adapted to the 90-degree lens. The “top-of-the-line” IR camera used cannot be equipped with wider-angle lens. By adding more identification points the matching problem can be eliminated.

4.2.2 Measuring size of cooled spots

It is seen in the figures presented earlier that the boundary between the cool and warmer area is not sharp. One reason is that the water spreads over the rock surface in addition to the seepage induced by gravity. The water is cooled as it spreads and will thus cause the temperature difference to air temperature to become smaller with increasing distance from the influx location. To estimate the size of the cool areas these were enclosed with a rectangle chosen subjectively in size and shape.

[2] The fraction of energy emitted as IR radiation compared to that from an ideal black body.

An example is given in Figure 2-1 where two rectangles enclose two spots and the cooled area below them. The minimum, maximum and mean temperatures in the enclosed areas are measured as well as the heights and widths of the areas. Enclosing a larger area resulted in a lower mean temperature difference between air and film and vice versa. Some simple tests suggest that within reasonable bounds the error caused by selecting the size of the area is less that a factor of two.

4.2.3 Estimating channel widths

To estimate the width of the channel from which the water seeps it was attempted to better see the size by narrowing down the visual size of the spot by reducing the temperature range of the picture to 0.4 °C. Examples are shown in Figures 2-5, 2-6, 2-8 and 2-9. Figure 2-6 shows two sets of spots each with three spots that seem to lie on a straight line and are close together. This could be a case where they actually are in the same fracture and might be said to belong the same channel with somewhat variable effluent. The spot or "channel" width estimated in this way was often 2–5 times smaller than the width of the rectangle used to enclose the cooling region. Using the procedure with the narrow temperature interval sometimes led to smaller "dark blue" spots not to be detected. We deem the uncertainty in channels widths is on the order of a factor 2–5 when it is done as described above. It may also be that the actual "channel" width in several cases is very narrow and that only the spreading of the water film on the surface seems to increase the size. It must also be considered that the emerging water is warmer than the coldest temperature measured on the rock surface and that it only cools down to steady state temperature after some spreading and cooling. This was clearly the case for the three high flow spots with high water temperature. The widths of the "high flow" spots were easier to measure as they were visible to the eye.

4.2.4 Energy supply from air and rock

In our analysis it was found that most of the energy needed for evaporation comes from the rock and this is probably the most uncertain entity for determining the evaporation rate. The rate of energy supply from the rock depends on the size and form of the spots, the temperature distribution on the spot surface and that of the "dry" rock surface and the temperature distribution in the rock itself. The latter may well be influenced by the distance to and shape and size of nearby spots. Our present subjective estimate is that the error using the simple spherical conduction model could be around a factor 2–3.

4.3 Improvement possibilities

Considerable simplification can be obtained by taking IR and VL pictures with the same focal length lenses from the same location. This simplifies the superposition of IR found spots onto the fracture maps.

5 Conclusions

It is shown that IR photography can be used to locate and identify spots with even very low leakage flowrates of water in fractured crystalline rocks. The channel surface density CSD (number of channels per m^2 tunnels surface area) and the flowrate distribution of channels and possibly channels widths can be assessed, although with an uncertainty of possibly a factor of two to five.

Observations of inflow locations, frequencies and channel widths on a rock surface makes it significantly more likely to find narrow high-flow channels in fractured rocks than by boreholes. The presence of high-flow channels in the complex channel networks that constitute the flow conduits can lead to more rapid transport of solutes.

The explored method is very simple and intrinsically can be even more improved to achieve higher effectiveness. As the leakage-spot location can be directly coupled to mapped fractures and fracture zones in the tunnel it can give information for more detailed investigations at the leakage points. In particular, fracture orientation and 3D modelling of fracture network based on mapping data from RoCS system combined with infrared 3D tunnel model can give a better understanding of water flow in fractured rock.

6 References

SKB's (Svensk Kärnbränslehantering AB) publications can be found at www.skb.com/publications.

Abelin H, Birgersson L, Gidlund J, Neretnieks I, 1991. A large scale flow and tracer experiment in granite i. experimental design and flow distribution. Water Resources Research 27, 3107–3117.

Bird R B, Stewart W E, Lightfoot E N, 2002. Transport phenomena. 2nd ed. New York: Wiley.

Carslaw H S, Jaeger J C, 1959. Conduction of heat in solids. 2nd ed. Oxford: Clarendon.

Finsterle S, Pruess K, 1995. Solving the estimation-identification problem in two-phase flow modeling. Water Resources Research 31, 913–924.

FLIR-T620-T640-Manual.pdf. Downloadable from FLIR Homepage. https://www.instrumart.com/assets/FLIR-T620-T640-Manual.pdf

Gylling B, Moreno L, Neretnieks I, 1999. The Channel Network Model – A tool for transport simulation in fractured media. Groundwater 37, 367–375.

Joyce S, Simpson T, Hartley L, Applegate D, Hoek J, Jackson P, Swan D, Marsic N, Follin S, 2010. Groundwater flow modelling of periods with temperate climate conditions –Forsmark. SKB R-09-20, Svensk Kärnbränslehantering AB.

Magnor B, 2004. Äspö Pillar Stability Experiment. Geological mapping of tunnel TASQ. SKB IPR-04-03, Svensk Kärnbränslehantering AB.

Monteith J L, Unsworth M H, 2007. Principles of environmental physics. 3rd ed. Burlington: Academic Press.

Neretnieks I, 2004. Predicting solute transport in fractured rocks- processes, models and some concerns. In Stephansson O, Hudsin J A, Jing L (eds). Coupled thermo-hydro-mechanical-chemical processes in geo-systems: fundamentals, modelling, experiments and applications. Kidlington: Elsevier, 19–30.

Neretnieks I, 2017. Solute transport in channel networks with radial diffusion from channels in a porous rock matrix. SKB R-15-02, Svensk Kärnbränslehantering AB.

Neretnieks I, Liu L, Moreno L, 2010. Mass transfer between waste canister and water seeping in rock fractures. Revisiting the Q-equivalent model. SKB TR-10-42, Svensk Kärnbränslehantering AB.

Perry R H, Green D W, 1997. Perry's chemical engineers' handbook. 7th ed. New York: McGraw-Hill.

SKB, 2014. Äspö Hard Rock Laboratory. Annual report 2013. SKB TR-14-17, Svensk Kärnbränslehantering AB.

Tsang C-F, Neretnieks I, 1998. Flow channeling in heterogeneous fractured rocks. Reviews of Geophysics 36, 275–298.

Tsang C-F, Neretnieks I, Tsang Y, 2015. Hydrologic issues associated with nuclear waste repositories. Water Resources Research 51, 6923–6972.

van Genuchten M T, 1980. A closed-form equation for predicting hydraulic conductivity of unsaturated soils. Soil Science Society of America Journal 44, 892–898.

Appendix A

Using evaporative cooling to measure flowrates from channels in fractures in rocks

Ivars Neretnieks, Longcheng Liu, December 2015, revised November 2017

Summary

Water that seeps from channels in fractures to a face of rock, e.g. in ventilated drifts and tunnels, will evaporate if the air humidity is less than that of the seeping water on the rock's surface. When the seeping water forms a film that is cooled by evaporation the temperature difference between the dry rock and wet rock can be measured by infrared techniques including IR photography. The temperature difference can be used to estimate the evaporation flux. The photograph shows the width[3] of the channel and the total area that is cooled. This information can be used to estimate three important entities: Channel width, channel flowrate and the frequency of channels if a large area of rock face is photographed.

Different mechanisms influence the temperature difference between the cooled area and the dry area. These must be accounted for when translating the IR photo information to flowrate. One source of heat for evaporation is the air, which is also cooled. The other energy source is from the rock mass. This heat comes by conduction from far away rock but also from conduction between the adjacent dry and wet sections. Scoping calculations are presented that suggest that both sources must be considered and simplifying equations are derived that can be used to account for these processes. A complication is that the seemingly dry rock may be cooled because the rock matrix is porous and although it has very low hydraulic conductivity, capillary forces that develop by the drying of the micropores of the rock near the surface will by pull water towards the rock surface and cool also the seemingly "dry" areas somewhat. This must also be compensated for when using the measured temperature difference to determine the seepage rate from the channels. A way of estimating this effect is also presented.

It is shown that at high seepage rates from narrow (small width) channels the entire water flowrate may not have time to evaporate during the time the water film slowly moves downward to reach the drain. Then, as the IR photo identifies the location of the effluent spot, it can be isolated and the water collected and flowrate measured. In drifts that can be sectioned off, the humidity of the air, its temperature and flow velocity can be changed to increase or decrease evaporation rate over one to two orders of magnitude. This would make it possible to measure much higher and much lower flowrates by the IR technique. We also explore other methods that could be used to measure the flowrate of a film in situations where some of the seeping water reaches the drain and evaporative cooling no longer can give the desired information. It is based on measuring the seepage rate of the film by adding a spot or spots of dye. These spots can be followed as the film falls downward. This method has not been tested in the field yet but seems to be simple provided the dye spot movement can be followed. Scoping tests on a bedrock slab gave promising results.

A.1 Background and introduction

Channel network models require data on the channel characteristics and frequencies. There is no simple method today to obtain data on the frequency of channels, their widths and flowrates. This report explores some ideas on how to measure three mentioned quantities.

When the water escaping from the channel through the wall of a tunnel seeps down the wall, one can measure the flow directly by collecting it if the spots can be identified and isolated. Some flowrates are so large that the water can actually be seen to flow as a stream or drops. These can readily be collected. Most channels have lower flowrates. Often these channels cannot be detected

[3] A channel we visualise as a conduit having a length in the flow direction, an aperture, which is the distance between the two faces of the fracture and a width, which usually much larger than the aperture in the third direction. Both aperture and width can vary along the channel.

by the eye (Abelin et al. 1991). Most channels in low conductivity fractured rock seem to have so low flowrates that the water evaporates into the ventilation air in the tunnel. The evaporation cools the surface from which evaporation takes place. The cooling can be used to locate the channels by infrared techniques, IR. IR information can also be used to estimate the evaporation rate and thus the flowrate of the channel.

Infrared photography can be used to photograph the tunnel wall and measure surface temperature of the seemingly dry surface. One can see from the photo how large the cooled area is around a channel and also observe the number of channels per area. This provides a first rough measure of the width and frequency of channels. The evaporation rate can be obtained by modelling the heat transport from air and rock to the cooled area.

Figure A-1 shows two examples of IR pictures of a rock wall with channels from which water that seeps down the vertical rock wall is cooled by evaporation. The pictures show areas that are about 2 m wide.

The basic idea to use the IR information is very simple. The evaporation rate m_{evap} is proportional to the heat flow Q needed to evaporate the water. The heat can come from the air, Q_a and from the rock, Q_r. These heat fluxes are proportional to the cooled area, which can be seen in the IR pictures and the temperature differences between the cooled surface and the air and rock respectively. The air temperature can be measured using a normal thermometer and the wet and dry rock temperatures are taken from the IR pictures. In addition one needs to know the mass and heat transfer coefficients between air and wet surface and the geometry for heat conduction in the rock.

With this the flowrate of water due to evaporation can be assessed. When all seeping water has not evaporated e.g. the dripping water and water that flows down the rock face to the drain must be determined by other means. The IR method is expected to have its best use for the low conductivity rocks that host a repository for radioactive waste.

A.1.1 Transport mechanisms involved and structure of the report

To facilitate for the reader to grasp and digest the main processes involved and their potential importance each chapter begins with a short chapter summary and conclusions.

Channels in fractures in rock conduct water out to the tunnel wall. From many channels the water flows down the rock wall as a thin film. At least part of the water evaporates into the air flowing in the tunnel. The evaporation cools the air as well as the rock. At low channel flowrates the liquid water never reaches the tunnel wall directly by the channel. It partly evaporates already in the micropores of the rock, also cooling the rock and water locally. In the partly saturated pores of the rock matrix, water is pulled by the strong capillary forces towards the rock surface. The water vapour also diffuses in the partially saturated micropores towards the tunnel. The vapour pressure of water is well below atmospheric pressure and the vapour transport is negligible compared to that of the liquid water in the micropores.

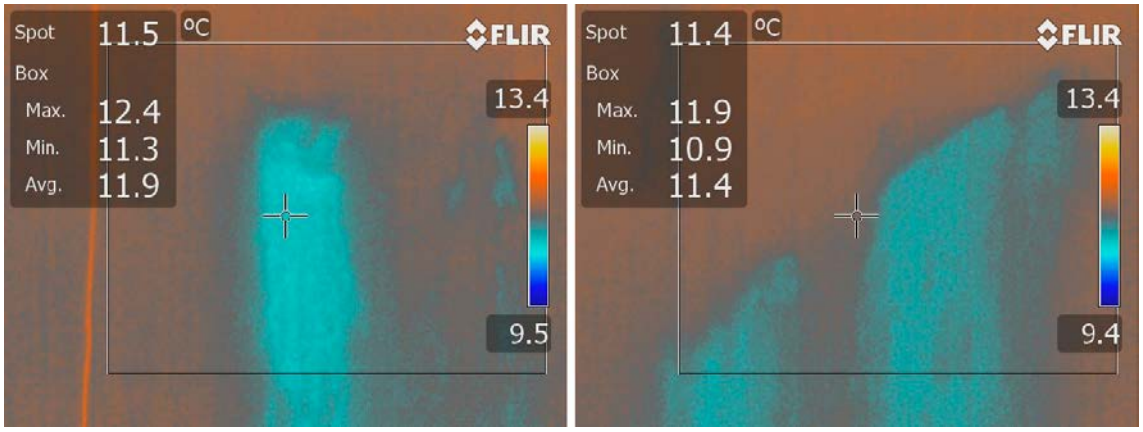

Figure A-1. *Picture number IR 458 and IR 464.*

Two main cases are considered and presented in two separate chapters. In the first, water from the channel reaches the rock surface, forms a film and seeps downward along the surface and evaporates, cooling the surface. In the second chapter the water is transported in the un-fractured rock matrix by capillary suction in addition to flow driven by the hydraulic head. Unsaturated flow is more complex to describe than saturated flow and warrants a separate treatment.

A.2 Water from a channel forming a film on the rock wall

A2.1 Chapter overview and summary

In this chapter we primarily treat the case where water seeps out from a channel and flows downward along the wall of the tunnel in a thin film. Air flows in the tunnel, evaporates water and transports it away as vapour. The air supplies some of the energy needed for the evaporation and cools the water in the film and the rock. The rock also supplies heat to the film by conduction. Water also moves through the rock matrix but in this chapter is neglected assuming that the low permeability of the rock will permit a marginal flowrate compared to the water coming directly from the channel.

Fundamental mass and energy balances are central to the supply of energy for the evaporation. Mass transfer rates between air and the evaporating wet area are determined by the air velocity set by ventilation but also by air movement generated by the density gradients in the air near the surface caused by evaporation. Both forced and free convection effects are found to contribute. It is further found that heat supply by conduction through the rock must be accounted and also that one must consider cases where the distance between nearby seeping channels is small and where it is large. To avoid the need for full three dimensional modelling of the rock around all seeping channels two simple computational schemes are proposed, one for sparse and one for dense channel locations. In this chapter it is also shown how ventilation rate, yearly temperature variations and distance from ventilation tunnel inlet can be expected to influence rock and air temperature at the location studied.

A2.2 Mass and energy balances

In both cases heat (energy) is transported in the rock by conduction in the rock matrix and by flow of liquid, vapour and gas. Conduction entirely dominates the heat transport from the rock interior to the surface. At the rock/air interface heat from the (warm) air also supplies heat for evaporation.

In the other situation, Section A.3, water seeps through the rock matrix because the water that evaporates at the rock surface also evaporates some water in the porous rock matrix and partially saturated conditions develop in the pores. This generates very strong capillary forces pulling liquid water towards the rock surface. The pressure gradient near the surface can become very large, much larger than the saturated hydraulic head in the rock and it can dominate the water flow in the partially saturated rock matrix. The temperature in the tunnel and air is typically below ambient. The water vapour content in the air is very low and vapour diffusion in the partially saturated pores is negligible compared to the rate of liquid water transport. Similar to the previous situation evaporation heat is supplied from the air as well as from the rock. In Section A.3 Figure A-19 shows this situation.

We mainly consider steady state, SS, conditions in most cases although some consideration is given to the rate of approach to SS.

A2.3 Cooling of flowing film from channel in fracture

Figure A-2 shows the situation when water emerges from a channel, W wide, onto a semi-vertical wall in a tunnel. The water forms a film, which flows down the wall. As it moves down the wall it evaporates and takes the energy from the air and from the rock and cools to a temperature T_f. We want to calculate the temperature of the water film (wet rock surface) and how it depends on a number of conditions including temperature and humidity of approaching air, air flowrate and temperature of rock far from the tunnel. To begin with we neglect vertical and horizontal heat conduction parallel to the wall between cold and warm area. Later we estimate this heat transport and show that is has some but not overly large effect.

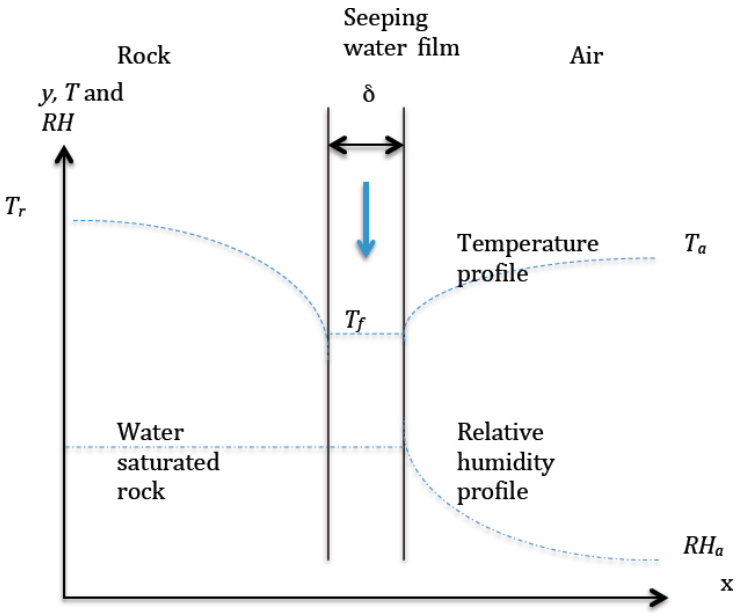

Figure A-2. *Evaporation from falling film by heat from rock as well as from air.*

The following equations are used to calculate the vapour pressure and moisture content of air at different temperatures with t in °C. The notation symbols are summarised in Section A.8.

Water vapour pressure for temperatures between 0 and 100 °C is well fitted by the Tetens equation (Monteith and Unsworth 2007).

$$p_v(t) = 610.78 * \text{Exp}(\frac{\text{t}}{\text{t} + 238.3} * 17.2694) \text{ Pa (t in }^{\circ}\text{C)} \quad \text{(A-1)}$$

The vapour density is then obtained from (A-1) and the gas law

$$\rho_v(t) = \frac{M_w}{R}\frac{p_v(t)}{(t+273.15)} = 0.002165\frac{p_v(t)}{t+273.15} \text{ kg/m}^3 \quad \text{(A-2)}$$

Energy and mass balances are set up as follows

The energy balance neglecting that carried by the flowing water itself is

$$Q_r + Q_a = Q_{evap} \quad \text{(A-3)}$$

Where Q_r is the rate of energy transport from the rock, Q_a that from the air and Q_{evap} is the energy used for evaporation.

The above entities can be obtained from

$$Q_r = -\lambda_r W_f dy \frac{dT}{dx}\Big|_{x=o} \quad \text{(A-4)}$$

$$Q_a = h_a W_f dy (T_a - T_f) \quad \text{(A-5)}$$

$$Q_{evap} = \Delta H_w m_{evap} \quad \text{(A-6)}$$

$$m_{evap} = Q_{evap} / \Delta H_w \quad \text{(A-7)}$$

W_f is the width of the film and dy a section of its height.

$\rho_v(T_f)$ is equilibrium vapour density at film temperature T_f

$\rho_v(T_a)$ is equilibrium vapour density at T_a.

m_{evap} is the rate of water evaporation [kg/s]

The heat and mass transfer coefficients are obtained by (A-8) and (A-9) from Bird et al. (2002, p 435, 678). They are commonly described by the dimensionless numbers $Nu = \frac{h_a\, d_t}{\lambda_a}$ and $Sh = \frac{k_m d_t}{D_a}$ repectively. The characteristic length in Nu and Sh is the tunnel diameter d_t for flow in a tube (tunnel).

$$h_a = Nu\frac{\lambda_a}{d_t} = \frac{\lambda_a}{d_t} 0.023\, Re^{0.8} Pr^{1/3} \quad \text{(A-8)}$$

$$k_m = Sh\frac{D_a}{d_t} = \frac{D_a}{d_t}\, 0.023\, Re^{0.8} Sc^{1/3} \quad \text{(A-9)}$$

where

$Re = \frac{u_a\, d_t \rho_a}{\eta_a}$, $Pr = \frac{\eta_a c_{p,a}}{\lambda_a}$ and $Sc = \frac{\eta_a}{D_a \rho_a}$

Equations (A-8) and (A-9) are valid for Re > 10 000. For the temperature range and tunnel diameters of interest in this study this implies air velocities above about 0.03 m/s. The equations apply for smooth walled tubes and tube lengths longer than some tens of tube diameters.

Figure A-3 shows how the heat transfer coefficient varies with air velocity.

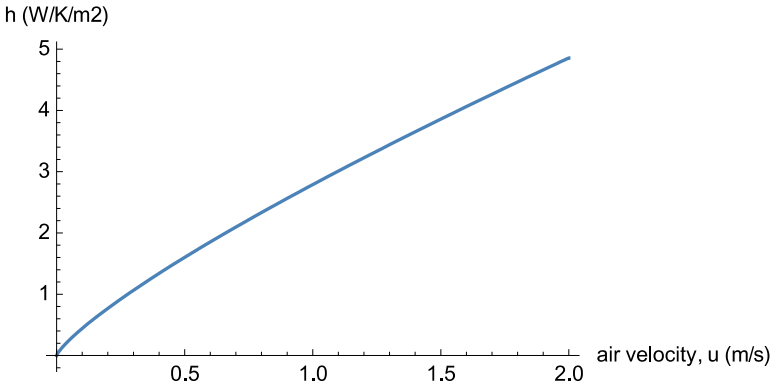

Figure A-3. *Heat transfer coefficient as function of air velocity for turbulent flow, Equation (A-8). (Computer program[4]: Evaporation from a circular area heated from the rock.nb)*

At low velocities free convection becomes important. Similarly for free convection on a vertical surface heat and mass transfer coefficients can be obtained from the following expressions (Bird et al. 2002, p 348 and 600). The characteristic length in Nu and Sh is the height of the film H in this case, not the tunnel diameter.

$$h_a = Nu\frac{\lambda_a}{H} = \frac{\lambda_a}{H} 0.518\, (Gr_T \mathrm{Pr})^{0.25} \quad \text{(A-10)}$$

$$k_m = Sh\frac{D_a}{H} = \frac{D_a}{H}\, 0.518\, (Gr_m \mathrm{Sc})^{0.25} \quad \text{(A-11)}$$

[4] This refers to the name of the computer program used to facilitate future retrieval.

$$Gr_T = \frac{\rho_a{}^2 g\, \beta_T \Delta T H^3}{\eta_a{}^2},\ \beta_T = \frac{1}{\rho_a}\frac{d\rho_a}{dT} = -\frac{1}{T} \cong -3.5\ 10^{-3} kg\ m^{-3}\ K^{-1}$$

the thermal expansion coefficient, ΔT the temperature difference between air and surface. H is the height of the section. ρ_a is the air density.

Similarly $Gr_m = \frac{\rho_a{}^2 g\, \beta_m \Delta \rho_v H^3}{\eta_a{}^2}$ and $\beta_m = \frac{d\rho_a}{d\rho_v} = -\frac{M_{Air} - M_w}{M_w} \sim -0.61$

As an alternative to using the heat transfer coefficients the mass transfer coefficients Equations (A-9 and A-11) together with a driving force based on vapour concentration can be used. Then the vapour concentration in the air and at the film surface must be also known.

The above equations are used below to estimate an expected range of values of heat transfer coefficient and temperature differences under different conditions. This will help planning the evaluation and interpretation of the IR pictures.

Figure A-4 shows how the heat transfer coefficient varies with temperature difference between air and film for different heights H of the cooling film.

When all energy for evaporation is taken from the air $Q_a = Q_{evap}$ and after some restructuring of the equations and utilising the definitions of Pr and Sc the following is obtained (Bird et al. 2002, p 684)

$$T_f = T_a - \left(\left(\rho_v(T_f) - \rho_v(T_a) RH\right) \frac{\Delta H_w}{\rho_a c_{p,a}} \left(\frac{Pr}{Sc}\right)^{2/3}\right. \qquad \text{(A-12)}$$

The value of group $\frac{\Delta H_w}{\rho_a c_{p,a}} \left(\frac{Pr}{Sc}\right)^{0.667} = 2\,280$ for the temperature range of interest for the case of turbulent flow in the tunnel. For free convection a similar expression is found

$$T_f = T_a - \left(\rho_v(T_f) - \rho_v(T_a) RH\right) \left(\frac{\Delta H_w}{\rho_a c_{p,a}}\right)^{4/5} \left(\frac{Pr}{Sc}\right)^{3/5} \qquad \text{(A-13)}$$

When the only source of heat for evaporation comes from the air the air velocity does not influence the results because the heat and mass transport coefficients depend on velocity in the same manner. However, it may be noted that the heat flux and evaporation rate per unit area changes by a factor of 6.3 when the air velocity is changed by a factor of 10.

Figure A-5 shows how the water film temperature changes with the air temperature for two different relative humidities of the air. The water film temperature is practically independent of the air flowrate if no heat is supplied from the rock. When heat, in addition, is supplied from the rock the situation becomes more complicated as shown in the following sections.

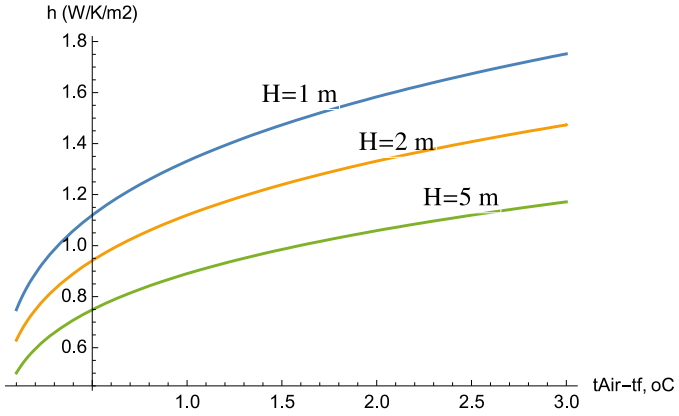

Figure A-4. *Heat transfer coefficient for free convection as function of temperature difference between air and film for different heights H of the cooling film, Equation (A-10). (Computer program: Evaporation from a circular area heated from the rock.nb)*

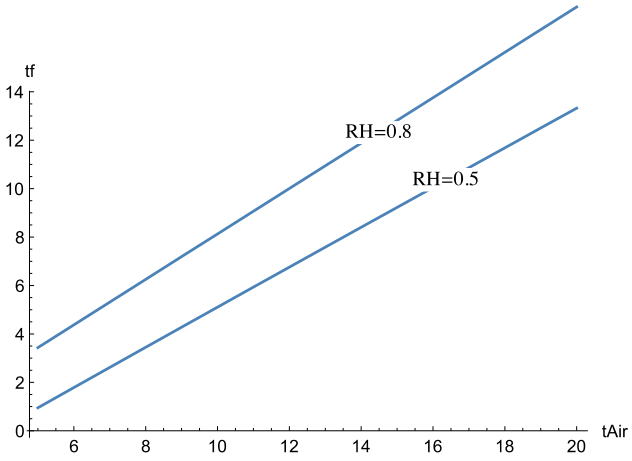

Figure A-5. *Water film temperature as function of air temperature for two different relative humidities, RH, in the air, Equation (A-13). (Computer program: Evaporation from a circular area heated from the rock.nb)*

The rate of evaporation and of heat transport, is proportional to $u^{0.8}$ as can be seen in Equations (A-8) and (A-9) and Figure A-6. This figure shows the heat flux from air to water film as function of temperature difference between air and film for two different air velocities.

Figure A-7 shows the mass flux of evaporating water from water film to air as function of temperature difference between air and film for two different air velocities.

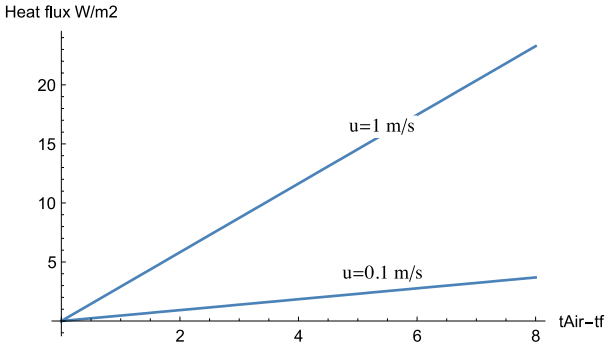

Figure A-6. *Heat flux from air to water film as function of temperature difference in °C between air and film, Equation (A-5 and A-8). Computer program:Evaporation and cooling.nb)*

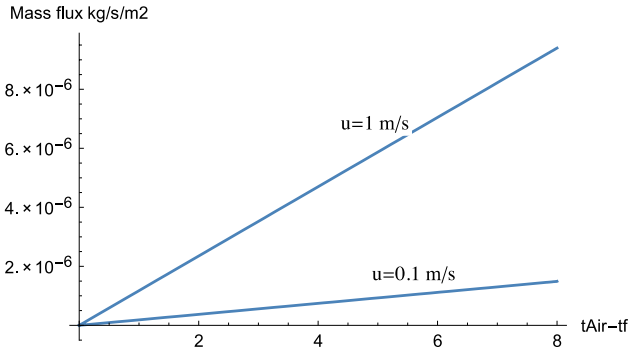

Figure A-7. *Mass flux from water film to air as function of temperature difference in °C between air and film, Equation (A-7). Computer program:Evaporation and cooling.nb)*

A2.4 Heat flow from rock

In this section we present some estimates of the magnitude of the heat flux from the rock to the cooling water film to compare it with the heat flux from the air. Also the heat flux from the dry areas of the rock to the nearby cool areas is estimated. The tunnel is idealized to be a long cylinder with diameter d_t ventilated with air with temperature T_a. The heat transport in the rock is described by the Fourier equation using cylindrical coordinates. First we wish to explore to what distance into the rock seasonal variations influence the rock temperature.

$$\frac{\partial T_r}{\partial t} = \frac{D_T}{r}\frac{\partial}{\partial r}\left(r\frac{\partial T_r}{\partial r}\right) \tag{A-14}$$

After excavation of a tunnel in the rock in which the temperature is T_o the initial condition is

$$\text{IC: } T_r(0,r) = T_o \tag{A-15}$$

The boundary conditions are that far into the rock the temperature remains at T_o

$$\text{BC1: } T_r(t, r \to \infty) = T_o \tag{A-16}$$

At the rock surface there is heat transfer to or from the rock from the ventilation air. This changes with the seasons, (A-17a).

$$\text{BC2a: } \left.\frac{\mathrm{dT_r}}{\mathrm{dr}}\right|_{\mathrm{r=r_t}} = -\frac{h_a}{\lambda_r}\left(\mathrm{T_a(t)} - \mathrm{T_r}|_{\mathrm{r=r_t}}\right) \text{ where there is NO water film} \tag{A-17a}$$

Another case treated later when the rock's surface is cooled by evaporation is with the boundary condition

$$\text{BC2b: } T_r(t, r = r_t) = T_f \text{ where there IS a water film} \tag{A-17b}$$

Analytic and numeric solutions of Equations (A-14) to (A-17) are used to study the heat flux to/from the rock and how ventilation flowrate and yearly changes of ventilation air temperature may influence heat transport from/to the rock and how this may influence to evaluation of the IR pictures.

Temperature of the dry rock surface and heat flux (BC2a)

In the parts of the tunnel where there is no water film we first study how the rock temperature evolves over time after the excavation of the tunnel and how it varies over the year when the air temperature changes. In this example air temperature varies sinusoidaly over the year with daily average minimum of −2 and maximum of 13 °C. This is about what the conditions are in the Oskarshamn area. The rock temperature far from the tunnels is T_o = 15 °C at repository depth in this example. The tunnel was excavated in the autumn (in the example) and is constantly exposed to fresh air flowing with the velocity 2 m/s.

Figure A-8 shows how the temperature in the rock varies over time and radial distance from the wall. It is seen that the temperature at the surface of the wall varies over time but on average over the year is very close to the temperature far into the rock. It is seen that the temperature variations over time are very small.

Figure A-9 shows the heat flux to and from the rock wall as it varies over the cycles of the year. The dry rock surface temperature is very near to that at the prevailing temperature in the rock at the depth. This is caused by the very large heat capacity of the larger mass of rock that evens out the effects of the "rapid" seasonal variations of the air.

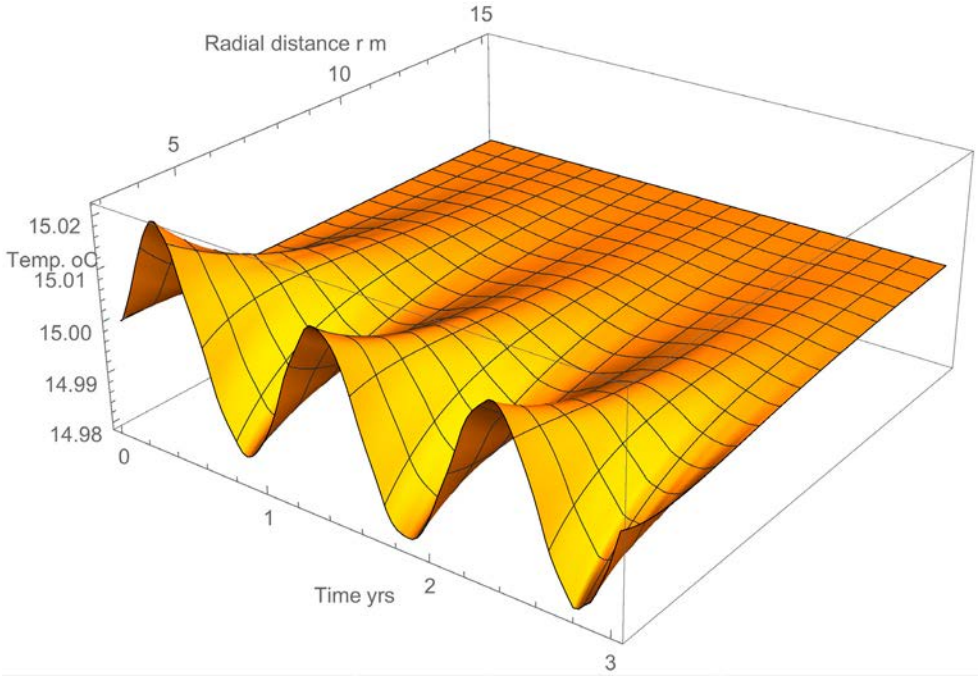

Figure A-8. *Temperature in the rock as it varies over time and radial distance from the wall. (Computer program: Tunnel temperature over years II.nb)*

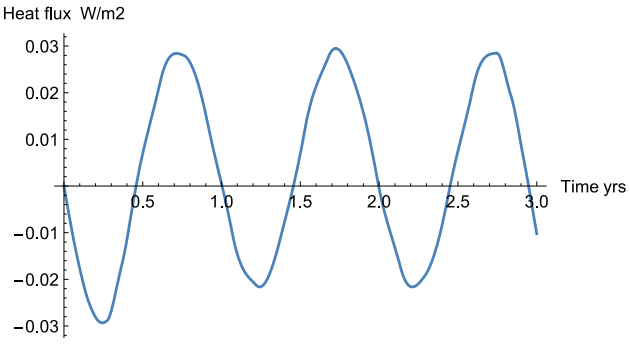

Figure A-9. *Heat flux over the rock surface variation over years. (Computer program: Tunnel temperature over years.nb)*

The temperature of the flowing air also changes as it flows along the tunnel and is cooled or heated by the rock. This can be described by the following equation based on the energy balance of the flowing air as it exchanges heat with the rock along the tunnel in the flow-direction z

$$\frac{\partial T_a}{\partial t} = -u_a \frac{\partial T_a}{\partial z} + \frac{\lambda_r}{\rho_a c_{p,a}} \frac{2}{r_t} \frac{\partial T_r}{\partial r}\bigg|_{r=r_t} \qquad \text{(A-18)}$$

The initial condition is that the rock has a constant temperature T_o. The boundary conditions are that 1) this temperature is maintained at large distance into the rock and 2) that the air temperature along the tunnel is equal to the surface temperature of the rock at the air/rock interface. The latter condition implies that there is no heat transfer resistance between air and rock in this example case. In order to be able to use a simple analytical solution the conduction in the rock is modelled as linear, which is permissible when the thermal penetration depth is not much larger than the diameter of the tunnel. This is not entirely satisfied but is acceptable for the present scoping calculations where we wish to see how fast the air approaches the rock temperature at depth T_o.

The solution is (Carslaw and Jaeger 1959)

$$\frac{T_a(t,z)-T_o}{T_{a,In}-T_o} = Erfc\left(\frac{z}{u_a}\frac{F}{\sqrt{D_T}\sqrt{t-\frac{z}{u_a}}}\right) \quad \text{(A-19)}$$

where t is time, $D_T = \frac{\lambda_r}{\rho_r c_{p,r}}$ the thermal diffusivity of the rock and $F = \frac{\lambda_r}{r_t \rho_a c_{p,a}}$. Figure A-10 shows how the temperature difference between air and rock evolves over time and along a tunnel for three different air velocities, 1, 0.3 and 0.1 m/s, clockwise from upper left.

The time scale in the example is chosen so that it is comparable to the seasonal changes. This implies that if the temperature in a tunnel at a certain distance along the tunnel is equal to that of the rock, also seasonal changes will not change it.

Figure A-11 shows the air temperature along the tunnel after 1 000 hours for three different air velocities, remembering that there is no heat transfer resistance between air and rock in this example case.

It is seen that the air temperature can not be expected to rapidly attain the far away rock temperature even at long distances along the tunnel except for very low air velocities because the seasonal inlet air temperature will have changed considerably over a few thousand hours. Therefore the dry rock surface temperature must be used to compare with the temperature of the cooling areas as well as the prevailing air temperature when the IR picture is evaluated. This is also supported by another simple approach to the estimate the evolution of the air temperature along the tunnel.

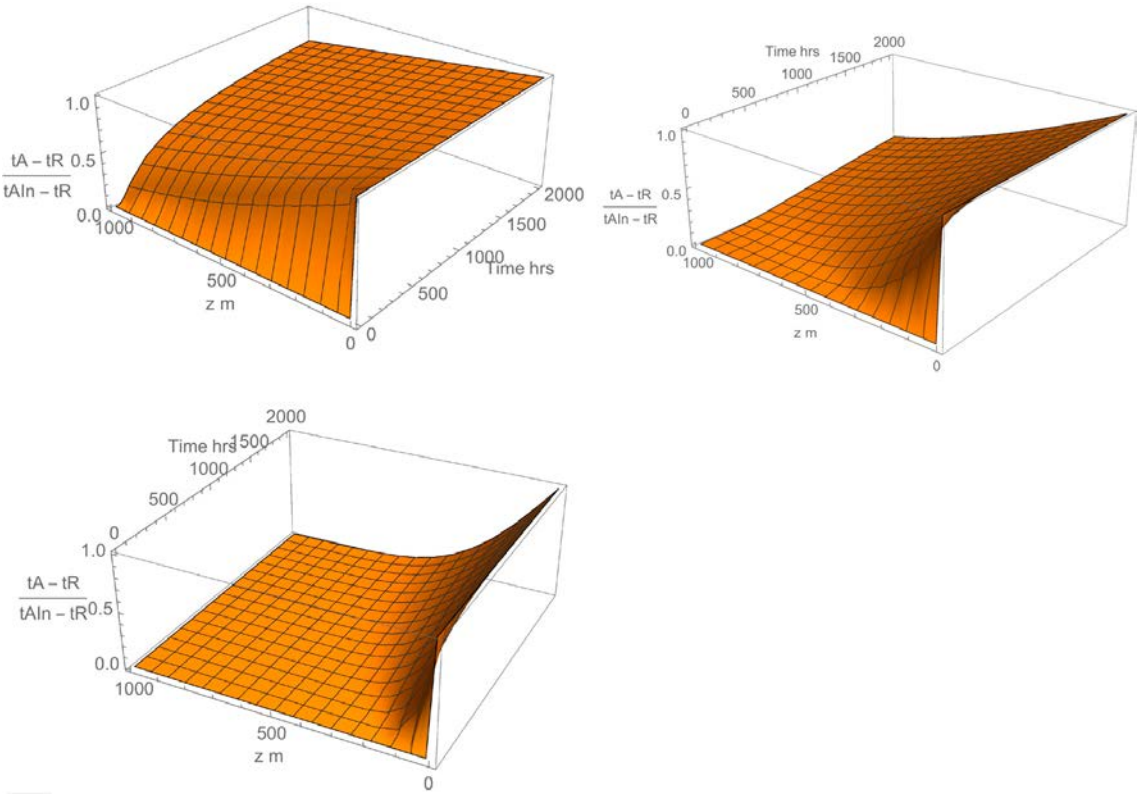

Figure A-10. *Relative temperature difference between air and rock as it evolves over time and along a tunnel when inlet temperature of air is constant. (Computer program: Tunnel temperature over years II.nb)*

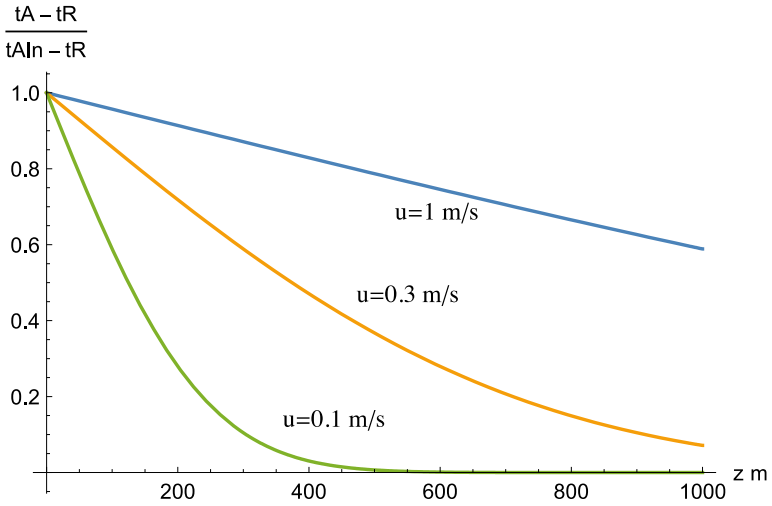

Figure A-11. *Air temperature along tunnel for three different air velocities. No heat transfer resistance in air but rock temperature nearest the surface changes over time. (Computer program: Tunnel temperature over years II.nb)*

Assuming in contrast to the previous analysis that the heat transfer resistance in the air dominates the evolution of the air temperature and that the rock surface temperature is maintained constant, the air temperature along the tunnel is obtained from

$$\frac{T_a(z)-T_o}{T_{aIn}-T_o} = (1 - e^{-Gz}) \qquad \text{(A-20)}$$

where

$$G = \frac{h_a}{c_{p,a}\rho_a r_t u_a} \qquad \text{(A-21)}$$

Figure A-12 shows the air temperature along the tunnel for three different air velocities assuming that the heat transfer resistance between air and rock dominates the rate of heat transfer and that the surface temperature of the rock is constant.

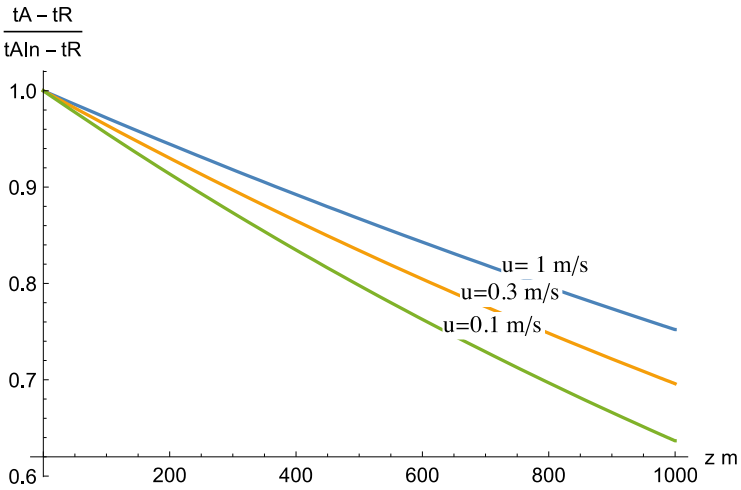

Figure A-12. *Air temperature along tunnel for three different air velocities. Heat transfer resistance in air but rock temperature at the surface is constant. (Computer program: Tunnel temperature over years II.nb)*

It is seen that for the highest air velocity the temperature along the tunnels resembles that for the previous case. For the lower velocities the differences become considerable. This can be foreseen looking at the "thickness" dr_a of an equivalent air "film" that would give the same heat transfer resistance, which is the inverse of the heat transfer coefficient $1/h_a$.

$$dr_a = \frac{\lambda_a}{h_a} \tag{A-22}$$

When dr_a is much smaller than the tunnel radius the resistance is small and can be neglected. When dr_a is larger than the tunnel radius the heat transfer resistance will dominate the temperature evolution of the air. For an air velocity of 1 m/s dr_a = 3 m, which is comparable to tunnel radius and the heat transfer resistance will have some impact. For an air velocity of 0.1 m/s dr_a = 19 m and the heat transfer resistance in the air cannot be neglected.

These scoping modelling results suggest that the heat transfer resistance in the air cannot be neglected when assessing the air temperature evolution over time and along the tunnel. We conclude that measurements of air temperature, air humidity and air velocity must be performed and documented for each IR picture.

Heat transfer in the rock between evaporation cooled and dry parts of the rock.

When a section of the tunnel is cooled by evaporation and the adjacent part is not, heat will be conducted by the rock between the regions. The warmer rock supplies heat to the region where evaporation occurs and increases the evaporation rate. We explore this effect here. Consider a wet tunnel section L wide adjacent to a long length of tunnel that is dry and thus warmer. The y-direction is into the rock and the x-direction is along the tunnel wall. A symmetric half section of the wet cold wall 0.5 m wide adjacent to a half section of dry rock 2.5 m wide is modelled. At x = 0 and at x = 3 m there are symmetry planes so that the setting is that every 6 meters along the tunnel there is a 1 m wide wet section in the middle.

The resulting steady state temperature is modelled by the Laplace equation, which describes the temperature distribution in the two dimensions. In the example, at the rock surface the temperature is 10 °C in the wet region and 15 °C in the dry region. Far into the rock (10 m) the temperature is 15 °C. At the symmetry planes x = 0 and x = 3 m there is no heat transport over the symmetry planes.

Figure A-13 shows the temperature distribution in the rock. Heat flows from the rock in both x- and y-directions towards the wet, cold, region. The mean temperature gradient at the wet surface is 4.3 °C/m in the direction into the rock. With a thermal conductivity of granite of 3 W/m/°C the mean heat flux to the wet region is 12.9 W/m^2. This is of the same magnitude as the heat flux from the air to supply energy for evaporation as will be shown later. This implies that heat conduction between cooled and dry areas must be accounted for when the rate of evaporation is assessed.

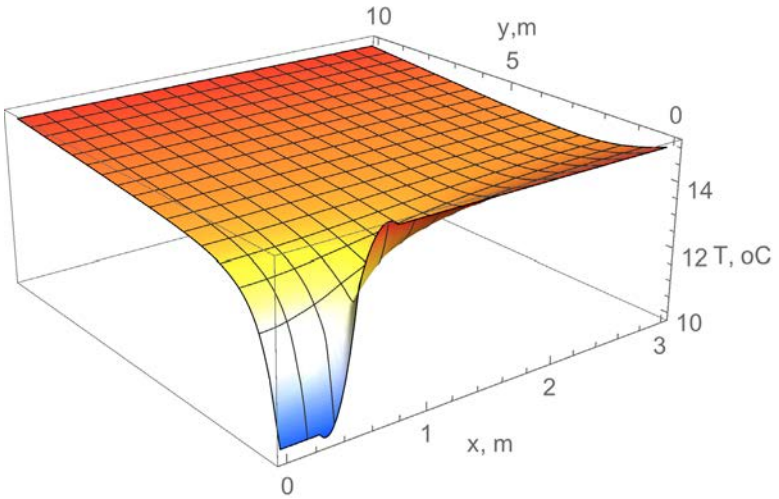

Figure A-13. *Temperature distribution in the rock when there is a wet cooling region adjacent to the dry rock. (Computer program: LaplacianSolution.nb)*

Evaporative cooling

It would be complicated to model a situation in detail, in three dimensions, when there are local effluent spots of different sizes that are unevenly distributed over the tunnel walls because it is necessary to account for all the spots and their cooling simultaneously. As can be deduced from inspection of Figures A-8 and A-13, spots or regions at distances smaller than about 10 m would influence each other, whereas spots at larger distance would not.

For a single spot with a distance larger than 10–20 m from other sports we propose a simplified approach based on the following. Approximate the area of the wet region by a circle with area $A_{spot} = \pi_{spot}^2$. We also utilise the relation that steady state conduction to/from a half-sphere, covering the spot, surrounded by a stagnant infinite medium can be described by the dimensionless heat transfer coefficient $Nu_{sph} = 2$ (Bird et al. 2002, p 439), where

$$Nu_{sph} = \frac{h_{sph} d_{sph}}{\lambda_r}$$

h_{sph} is the heat transfer coefficient to the sphere and d_{sph} is the diameter. We thus surround the cooled spot with a half-sphere of rock with the same temperature as that of the cool surface. Heat is conducted with spherical symmetry from the interior of the rock to the spherical surface.

Assuming for the present that the rock surface temperature at some distance from the cooling spot is equal to that far into the rock i.e. the rock surface without a cooling film $T_{r,s}$ is equal to the temperature of the rock far away T_o the heat transfer coefficient to the sphere is

$$h_{sph} = \frac{\lambda_r}{r_{sph}} \tag{A-23}$$

where

$r_{sph} = r_{spot}/\sqrt{2}$ is the radius of a half-sphere with the same area as A_{spot}.

In practice the infinite medium can be taken to start at a distance > $5d_t$. Then the error in h_{sph} is about 10 %.

For spots or regions closer than 10–20 m to other sports or other cooling regions another approach is used. When many spots lie close the heat conduction from the warmer region between the spots will dominate over the heat transport directly directed from the far away rock. We can visualise that transport to be evenly distributed over the entire cross section when at large distance and then, closer to the surface, it divides up to the individual spots that together make up a fraction φ of the cross section.

The mean temperature of the rock surface is

$$T_{r,s,mean} = T_{r,s}(1 - \varphi) + \varphi T_f \tag{A-24}$$

For radial conduction to the tunnel the heat flux $\frac{Q_r}{A}$ to the circular tunnel (Bird et al. 2002, p 307), again assuming that $T_{r,s}$ is equal to the temperature of the rock far away T_o.

$$\frac{Q_r}{A} = \frac{\lambda_r}{r_t \ln\left({r_{far}}/{r_t}\right)}\left(T_o - T_{r,s,mean}\right) = h_{cyl}(T_o - T_{r,s,mean}) = h_{cyl}\varphi(T_o - T_f) \tag{A-25}$$

The fraction of the area covered by the spots receives all the heat flow so

$$Q_{r,spot} = h_{cyl} A_{spot}(T_o - T_f) \tag{A-26}$$

The heat transfer coefficient defined over the area of a spot is

$$h_{cyl} = \frac{\lambda_r}{r_t \ln\left({r_{far}}/{r_t}\right)} \tag{A-27}$$

r_{far} is some far away distance to a boundary where the temperature is T_o. h_{cyl} is not very sensitive the value of r_{far}. We chose a value $r_{far}/r_t = 2.7$ which gives ln $r_{far}/r_t = 1.0$. We summarise that the heat transfer coefficients as used above for the two cases are

$$h_{sph} = \frac{\lambda_r}{r_{spot}} \text{ and } h_{cyl} = \frac{\lambda_r}{r_t}$$

This implies that when $r_{spot} < r_t\sqrt{2}$ the spot will receive more heat by the cylindrically radial conduction and this relation should be used. In practice this means that when the spot diameter is larger than tunnel diameter cylindrical heat transport will dominate the heat flow to the wet surface.

The heat transport from the rock to a spot is

$$Q_r = h_r A_{spot}(T_r - T_f) \tag{A-28}$$

Where h_r is either h_{sph} or h_{cyl}.

The energy balance for the cooling spot accounting for transport from air Q_a, evaporation Q_{evap} and conduction from rock Q_r becomes

$$Q_r + Q_a = Q_{evap} \tag{A-29}$$

Inserting the expressions for the three heat fluxes gives

$$h_r(T_r - T_f) + h_a\,(T_a - T_f) = k_m\,(\rho_v(T_f) - \rho_v(T_a)RH)\Delta H_{evap} \tag{A-30}$$

The only unknown in this equation is the film temperature T_f, which is readily obtained by solving the nonlinear equation numerically, or by a linear approximation as shown below.

To gain some insights into how important the heat from the rock is in relation to that from the air the relation $\rho_v\,(T_f)$ is linearised to

$$\rho_v(T_f) = \rho_v(T_a) + \frac{d\rho_v}{dT}(T_f - T_a) \tag{A-31}$$

around $T = T_a$. This is reasonable considering that the expected deviation of T_f from T_a is small, less than 6 °C, Equation (A-30) becomes

$$h_r(T_r - T_f) + h_a\,(T_a - T_f) = k_m\,\Delta H_{evap}\left(\rho_v(T_a) + \frac{d\rho_v}{dT}(T_f - T_a)\; - \rho_v(T_a)RH\right) \tag{A-32}$$

This linear equation has the solution

$$T_f = \frac{h_a T_a + h_r T_r + HK(T_a)\,T_a - k_m \Delta H_w (1-RH)\rho_v(T_a)}{h_a + HK(T_a) + h_r}$$

where $HK(T_a) = k_m \Delta H_w \frac{d\rho_v}{dT}$ (A-33)

Figure A-14 shows how the evaporation rate per area is influenced by the spot size.

Figures A-15 and A-16 show how the temperature difference between rock and water film and evaporation rate varies with air velocity and how these entities are influence by rock and air temperature and by relative humidity of incoming air.

It is seen in Figure A-17 that at low rock temperatures and high air temperatures condensation will occur. Figure A-18 shows that when air temperature is low and rock temperature is high considerable evaporation will result.

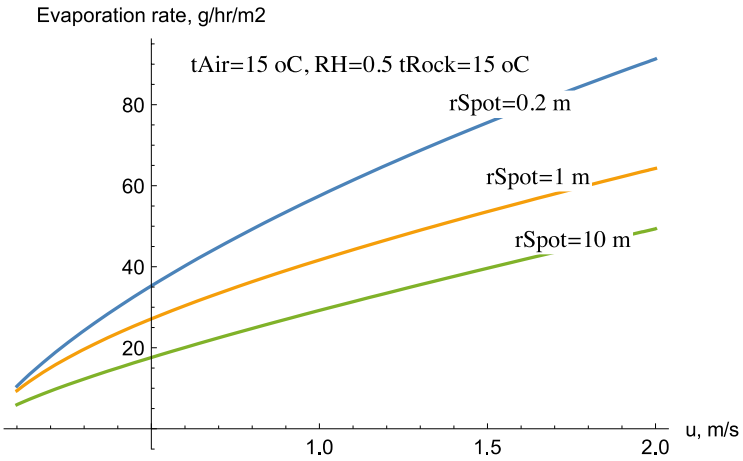

Figure A-14. *Evaporation rate for different sizes of wet spots when there is conduction from the rock. Air temperature is 15 °C, RH = 0.5 and rock temperature is 15 °C. (Computer Program: Equations for heat and mass transport, evaporation rates and film temperatures.nb)*

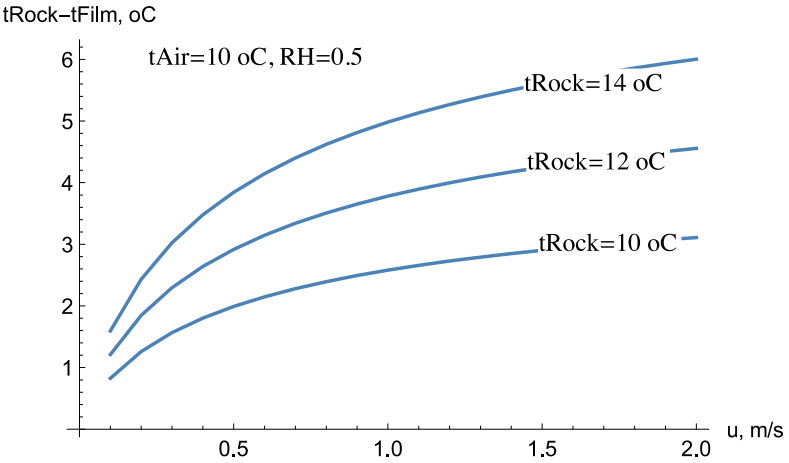

Figure A-15. *Temperature difference between rock and water film vs. air velocity for different rock temperatures. Air temperature is 10 °C and RH = 0.5, spot radius = 1 m. (Computer Program: Equations for heat and mass transport, evaporation rates and film temperatures.nb)*

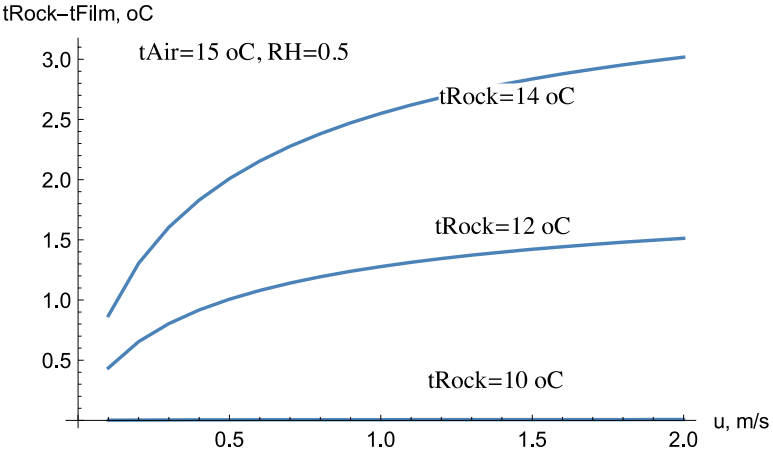

Figure A-16. *Temperature difference between rock and water film vs. air velocity for different rock temperatures. Air temperature is 15 °C and RH = 0.5, spot radius = 1 m. (Computer program: Equations for heat and mass transport, evaporation rates and film temperatures.nb)*

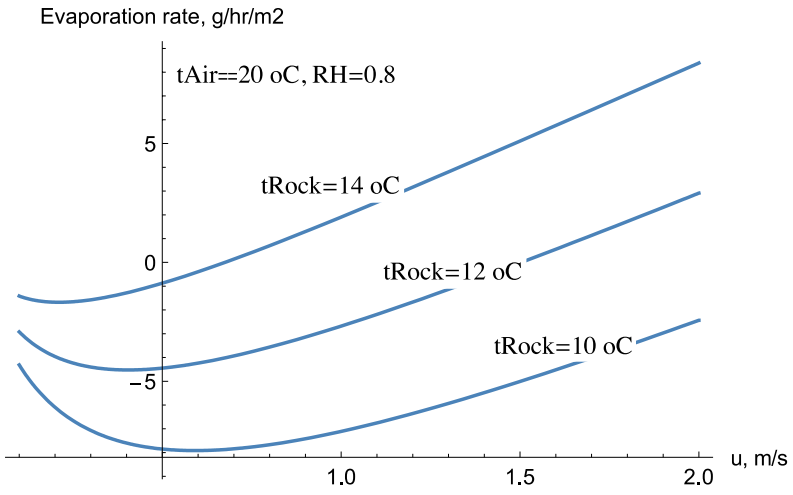

Figure A-17. *Evaporation/condensation rate vs. air velocity for different rock temperatures. Air temperature is 20 °C and RH = 0.8, spot radius = 1 m. (Computer Program: Equations for heat and mass transport, evaporation rates and film temperatures.nb)*

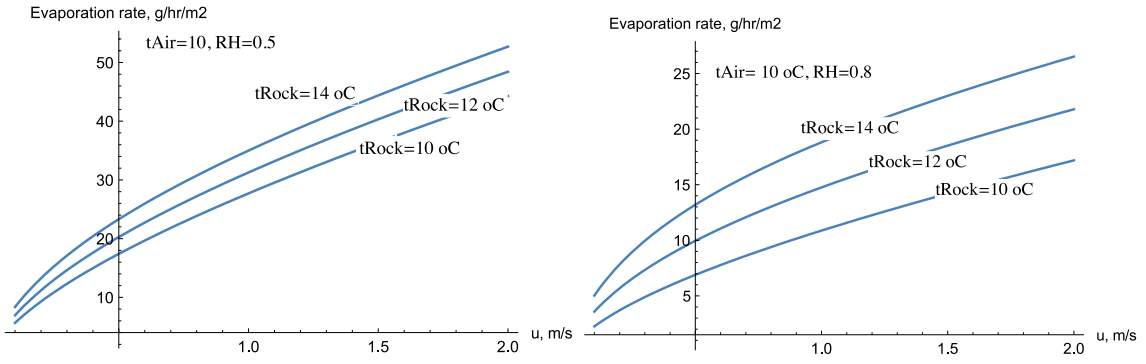

Figure A-18. *Evaporation rate vs. air velocity for different rock temperatures. Air temperature is 10 °C and RH = 0.5 left and RH = 0.8, right figure, spot radius = 1 m. (Computer Program: Equations for heat and mass transport, evaporation rates and film temperatures.nb)*

A.2.5 Tentative conclusions for Section A.2

These simple scoping calculations have shown that the evaporation rate depends in a complex way on many intertwined processes and entities. Air velocity, temperature and humidity can to some extent be controlled and could be used to increase or decrease evaporation if so desired. This would be valuable in validation experiments. Far away rock temperature and size of wet spots as well as surface "dry" rock temperature also influence the evaporation rate together with the previously mentioned entities in a complicated way and must be estimated or assessed by other means. Nevertheless, the prediction of evaporation rates seems to be "robust" in the sense that if air velocity, rock temperature and air temperature and relative humidity are accurately measured other factors such as spot size and form seem to give uncertainties on the order of a factor of two up and down on evaporation rate. However, further simulations and direct measurements validation simulations must be made to confirm this.

A.3 Water transport by capillary forces from rock matrix

A3.1 Chapter overview and summary

From the IR photographs the temperature of the moist rock surface as well as the temperature of the "dry" rock surface is determined. A question asked in this chapter and illustrated by modelling of capillary flow is if the "dry" rock surface actually can be assessed from the IR images. We explore

a situation when water seeps through the rock matrix. Then the water that evaporates at the rock surface also evaporates some water in the porous rock matrix and partially saturated conditions develop in the pores. This generates very strong capillary forces pulling liquid water towards the rock surface. The suction (negative pressure) gradient near the surface can become very large, much larger than the saturated hydraulic head gradient in the rock and it can dominate the water flow in the partially saturated rock matrix. It is shown that it is reasonable to use the measured rock temperature in the "dry" areas to represent that of the dry rock surface.

A3.2 Impact of capillary suction

The temperature in the tunnel and air is typically below ambient. Water vapour content in the air is very low and vapour diffusion in the partially saturated pores is negligible compared to the rate of liquid water transport aided by capillary forces. Similar to the previous situation evaporation heat is supplied from the air as well as from the rock. Figure A-19 shows this situation.

In this case only water seepage through the unfractured rock matrix is considered. This seepage will influence the rock surface temperature at seemingly dry places.

This case is similar to the previous but with the difference that there is no *water film* on the rock surface supplied by a flowing channel. All water seeps through the unfractured rock matrix pushed by a hydraulic head and pulled by capillary forces.

A3.3 Equations for unsaturated flow

For these exploratory calculations the equations are written for one dimension but can readily be expanded to two or three dimensions. Some simplifications are applied already here. The energy transport by the mobile liquid water, vapour and air are neglected on the grounds that the heat transport by thermal conduction is much faster. The movement of air and of water vapour in the pores is also neglected. The density and viscosity of liquid water, vapour diffusivity, thermal conductivity and heat capacity of the rock are taken to be independent of temperature.

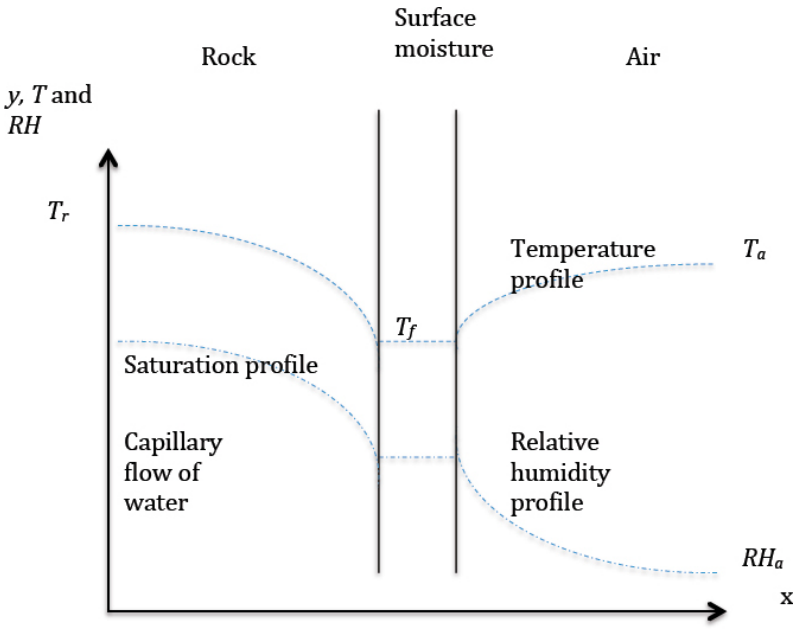

Figure A-19. *Evaporation of surface moisture by heat from rock as well as from air.*

The Richards equation is used to describe transport in the partially saturated rock matrix. Under such conditions strong capillary forces can contribute to the flux. When these dominate over the purely hydraulic head and gravity the water flux can be described by

$$J_y = \frac{k_o \rho_w}{\mu_w} k_{rel,w} \frac{dp_c}{dy} \quad \text{(A-34)}$$

Gas flow and transport is neglected. k_o is the permeability of the rock matrix, $k_{rel,w}$ is the relative permeability for water and p_c is the capillary (suction) pressure. $k_{rel,w}$ and p_c are complex functions of water saturation S. Very large suction pressures result at low saturation. The vapour pressure over the water over the capillary surface is less than that over a planar surface. The lowering of the vapour pressure is due to the lowering of the chemical potential of the water in the capillary subject to the surface tension forces that lower the energy of the water below (on the water side of) the meniscus. The relation between the vapour pressure, expressed as relative humidity and the capillary suction pressure is

$$p_c = \frac{RT}{V_w} \ln(RH) \quad \text{(A-35)}$$

Where $RH = \frac{p_v}{p_v^o}$, p_v the equilibrium vapour pressure over the capillary or in the partially saturated porous medium and p_v^o is the vapour pressure of unconfined water at temperature T.

The suction pressure can become very large already at RH slightly deviating from unity as can be seen by the value of $\frac{RT}{Vw}$, which at ambient temperature is 135 MPa.

Figure A-20 shows this relation.

At common relative humidities in air in contact with the rock wall there will be very large suction pressures pulling the water towards the rock surface where it can evaporate and be carried away by the air flowing in the tunnel. The hydraulic conductivity of the rock matrix for the partially saturated pores decreases with saturation and tends to counteract the effect of the high suction pressure on the water flux.

The water transport in porous medium for partially saturated conditions is described by Darcy's law:

$$J_w = -\frac{k_o \, k_{rel,w}}{\mu_w} \left(\frac{dp}{dx} - \rho_w g_x\right) \quad \text{(A-36)}$$

where p is the pressure gradient which also includes the suction pressure effects. g_x is the gravity vector component in the x-direction. The relation between the intrinsic permeability k_o and the hydraulic conductivity K is given by:

$$k_o = \frac{\mu_w}{\rho_w \, g} K \quad \text{(A-37)}$$

At room temperature, the intrinsic permeability k_o is thus approximately seven orders of magnitude lower than the hydraulic conductivity K (In SI units)

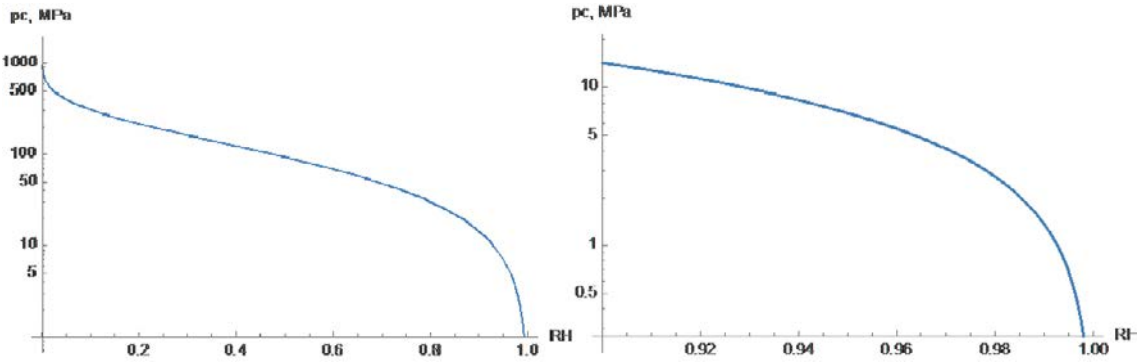

Figure A-20. *Suction pressure shown positive vs. relative humidity of the water vapour in the pores. The right figure shows a detail of the left. (Computer program: VanGenuchten and evaporation III.nb)*

The relative permeability is the ratio between the conductivity at unsaturated and saturated conditions and therefore has values between zero and unity. The latter value at saturated conditions. The relative permeability is a function of saturation. A commonly used relation is attributed to van Genuchten (1980), who also proposed a relation between the capillary or suction pressure p_c and the effective pore saturation S_e.

$$k_{rel,w}(S_e) = \sqrt{S_e}(1 - (1 - S_e^{\frac{1}{\lambda}})^{\lambda})^2 \tag{A-38}$$

$$S_e(p_c) = (1 + (\frac{p_{gas}+p_c}{P_o})^{\frac{1}{1-\lambda}})^{-\lambda} \tag{A-39}$$

$$S_e = \frac{S_w - S_{w,resid}}{1 - S_{w,resid}} \tag{A-40}$$

S_w is water saturation i.e. fraction of pore volume filled with water and $S_{w,resid}$, is the residual saturation. For the cases of interest here the gas pressure in the pores is very much smaller than the capillary pressure and is neglected. Note that p_c, although it is negative is defined positive in the formulas. We use the data proposed by Finsterle and Pruess (1995) in the examples with p_o = 1.74 Mpa, λ = 0.6, and $S_{w,resid}$ = 0.

Figure A-21 shows an example of suction pressure in granite vs. effective saturation at ambient temperature.

The water permeability of the partially saturated matrix is lower than for a fully saturated matrix by a factor $k_{rel,w}$, the relative permeability for water. Figure A-22 shows an example.

When, as in the case of present interest, the capillary forces are much stronger than other driving forces, including gravity, the water flux in the partially saturated region can also be written

$$J_w = -\frac{k_o\, k_{rel,w}}{\mu_w}\frac{dp_c}{dx} = -\frac{k_o\, k_{rel,w}}{\mu_w}\frac{dp_c}{dS_e}\frac{dS_e}{dx} = -D_c(S_e)\frac{dS_e}{dx} \tag{A-41}$$

D_c can be interpreted as a diffusion coefficient that depends on the saturation of the pores. The relation applies to water. A similar relation can be obtained for gas transport but we will neglect gas transport because is has negligible impact for the conditions of interest here.

Figure A-23 shows D_c as function of the effective saturation for the permeability $k_o = 10^{-19}$ m^2. This corresponds to a hydraulic conductivity $K = 10^{-12}$ m/s.

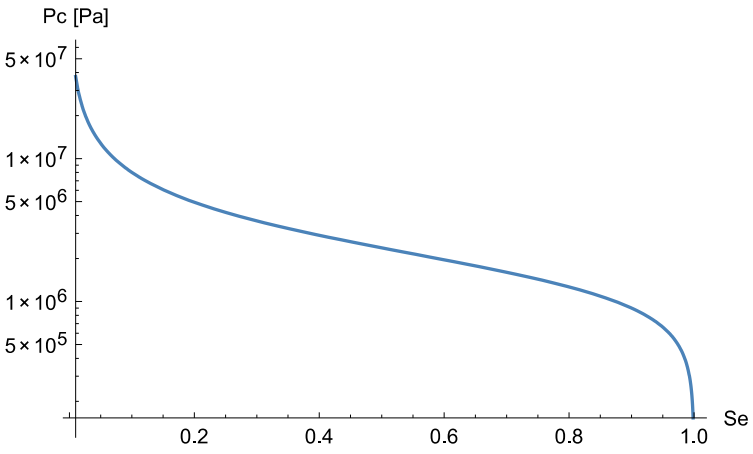

Figure A-21. *Example of suction pressure vs. saturation in granite. (Computer program: VanGenuchten and evaporation III.nb)*

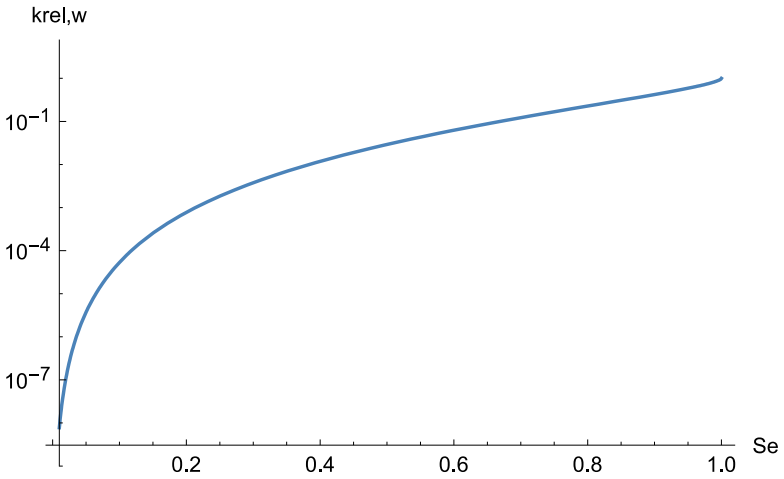

Figure A-22. *Example of relative permeability vs. saturation in granite, (Computer program: VanGenuchten and evaporation III.nb)*

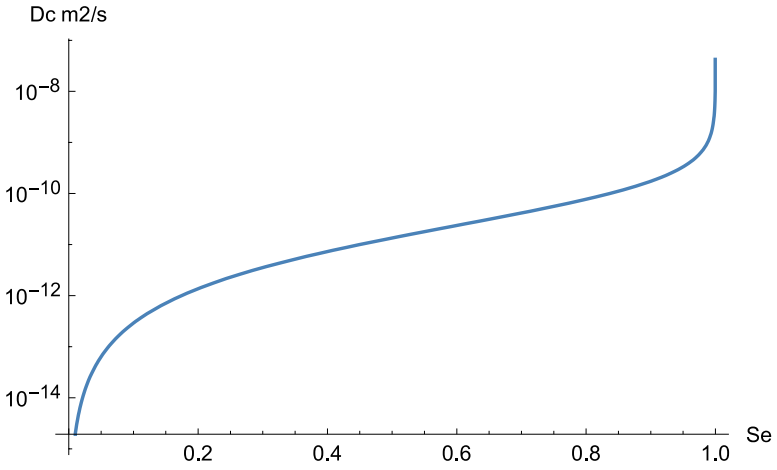

Figure A-23. *"Diffusion coefficient" of water in a partially saturated granite matrix. (Computer program: VanGenuchten and evaporation III.nb)*

In tunnels at depths of 100–500 m in saturated rock the hydraulic pressure is 1–5 MPa. The capillary pressure can be much larger at low saturations, but although the relative permeability then is lower, capillary induced flow must be considered as a potentially important transport process.

The steady state radial flux caused by hydraulic head differences to a circular tunnel can be described by the following equation when the hydraulic conductivity is constant K_w as assumed in this scoping calculation aimed at estimating the highest reasonably possible water flux through the matrix reaching the tunnel. The equation describes the flux driven by hydraulic head and by the capillary forces in the partially saturated rock matrix. At some (small) distance from the wall the gas pores are sufficiently connected to allow the water pressure to become equal to the air pressure in the tunnel. At that point the driving force for the water flow is equal to the suction pressure so the total head difference between that point and the head far away, i.e. the depth of the tunnel is

$$z_{tunnel} + \frac{p_c(Se_{gas})}{\rho_w\, g} \tag{A-42}$$

For radial flow the flux is

$$J_{w,max} = \frac{K}{r_t} \frac{(z_{tunnel} + p_c(Se_{gas})/(\rho_w\, g)}{\ln(\frac{r_{far}}{r_t})} \tag{A-43}$$

z_{tunnel} is the hydraulic head at the depth of the tunnel, p_c (Se_{gas}) is the capillary pressure at an effective saturation when the gas relative conductivity permits the gas to flow and allows the pressure in the pores to be the same as that in the tunnel. r_{far} is the distance to the far away boundary where this head prevails. This can be the distance to the ground surface, z_{tunnel}, or some other reasonably chosen distance that may be more appropriate when there are several nearby excavations. The equation is not very sensitive to the choice of r_{far}. Considering the impact of the uncertainties that the permeability of the rock matrix varies and that the rock also contains water conducting fractures, for the present scoping calculations we set $r_{far} = 2.7\ r_t$, which gives

$$\ln (r_{far} / r_t) = 1 \ln(\frac{r_{far}}{r_t}) = 1.$$

The saturation Se_{gas} at which the gas pores become connected is expected to be around 0.7 and then p_c (Se_{gas}) ≈ 1 MPa as can be seen in Figure A-21. Then $\rho_w\ g\ z_{tunnel} + p_c\ (Se_{gas}) \approx 6$ MPa for a tunnel at 500 m depth.

For $K = 10^{-12}$ m/s, which is a high value for the rock matrix, and a tunnel with diameter 5 m at 500 m depth the flux is $J_{w,max} = 2 \times 10^{-10}$ m^3/m^2/s or $J_{w,max}\ \rho_w = 0.72$ g/m^2/hr. This is deemed to be an upper bound of water flux through the matrix that can be supplied to the tunnel. This presumes that the water unhindered can pass the partially saturated zone near the surface where the relative conductivity is lower.

We now explore what driving force is needed to evaporate this flux of water

$$J_{w,max}\rho_w = m_{evap} = k_m \left(\rho_v(T_f) - \rho_v(T_a)RH\right) \quad \text{(A-44)}$$

With a mass transfer coefficient $k_m = 0.0024\ u_a^{0.8}$ m/s and $u_a = 1$ m/s the driving force $\rho_v\ (T_f) - \rho_v\ (T_a)\ RH = 0.08$ g/m^3. Considering that saturated air contains between 6 and 16 g/m^3 water vapour in the temperature range 0–20 °C this will give a minor evaporation resulting in the cooling of the emerging water by 0.2 °C if all the energy was taken from the water. It will be less if also the rock contributed to the energy.

From these scoping calculations it seems reasonable to assume that the measured rock temperature in the dry areas can be taken to represent that of the dry rock surface.

A.4 Estimation of water flowrate from channels using IR information – an example

A4.1 Chapter overview and summary

This chapter uses one IR picture to illustrate how the temperature differences and spot size can be used to estimate the seepage flowrate. It also illustrates how the IR pictures are documented using a protocol that describes the main data and location of the picture. The impact of air velocity and spot size on the resulting flowrate data also illustrates how uncertainties in the evaluated spot size and air velocity may influence the results. The example is chosen so that the reader will see that there are uncertainties that are difficult to eliminate if only IR information is to be used. However, once the location of the seepage location has been identified the seepage rate can be determined more accurately by collecting the water in the pinpointed location by collecting it a cloth and weighing. This has been called the diaper method.

A4.2 Illustrative example

From the IR pictures the size A_{spot} of the wet spot can be estimated visually or by some more sophisticated method using the detailed temperature data in the picture. This area is converted to r_{spot} via $A_{spot} = \pi r_{spot}^2$ and $r_{sph} = r_{spot}/\sqrt{2}$. It is assumed that the air velocity u_a and rock and air temperature T_r and T_a and the relative humidity RH of air are known. The evaporation flux J_{evap} is calculated and the total mass flowrate is obtained from $m_{evap} = J_{evap}\ A_{spot}$.

Considering the many assumptions and simplifications used to derive the expressions validation is needed. One test is to compare the measured temperature difference between dry rock and wet rock in the picture. This is compared to the modelled value. A small difference between predicted and observed would suggest that the results are reasonable. This, however, is not sufficient. There is a need to actually measure the flowrate of seeping water from the channel by collecting it. This can be done e.g. by covering the effluent spot, located and identified by the IR picture, by a plastic sheet glued onto the rock surface. The water is collected in the sheet. This has successfully been done on a large scale in an experiment in the Stripa experimental mine without unreasonable effort (Abelin et al. 1991). Other ways to measure the flowrate will be discussed in Section A.5 also.

Below we illustrate how the information in an IR picture can be used to estimate the evaporation rate. The example is from Äspö and a sample of the protocol information that accompanies each picture taken in 2013 is shown.

Every IR picture is accompanied by information in a protocol ledger. An example is shown below.

IR_0293.jpg, 2013-04-1, Tunnel Q, 450 m depth, Location in drift, distance (m): 3 500. Air temperature (°C):12.0.
Humidity (%): 67/77. Wind speed (m/s): < 1 m/s, Camera height over floor (m): 1.3.
Width of picture (m): 2.0 (L = 5.8)

Facing: ⊗ Left ○ up ○Right (In relation to positive distance axis along drift or tunnel, ⊗)

Visual estimation of area gave r_{spot} ~ 1 m. The wind speed was < 1 m/s, which was the lowest velocity our meter could detect.

The temperature of the "dry" rock is t_{Rock} = 11.9 °C taken from warmest place in the picture. Within the cooled area the mean temperature is taken to be the mean of 10.2 and 9.4 °C i.e. 9.8 °C. The temperature difference between dry and wet area then is $t_{Rock} - t_{Film}$ = 2.1 °C.

Figure A-24 was chosen to illustrate some of the uncertainties in determining the temperatures from just a single picture. It suggests that a larger area must simultaneously be considered to accurately determine what the dry rock temperature as well as the cooled area temperature is. The situation is much simpler when the cooled area is more clearly different from the dry area as in the two pictures shown earlier in Figure A-1.

There are further uncertainties in evaluation the evaporation rate we wish to point out. As was shown earlier, the size of the spot and the presence of nearby spots, not considered in this example, influences the evaporation rate also if the local temperature difference is accurately determined.

In Figure A-25 for a spot with 1 m radius the predicted temperature difference is smaller than if the cooling area is larger, Figure A-26, or if it contains many spots at close distance. The figures also show that it is necessary to know the air velocity accurately as this strongly influences the evaporation rate.

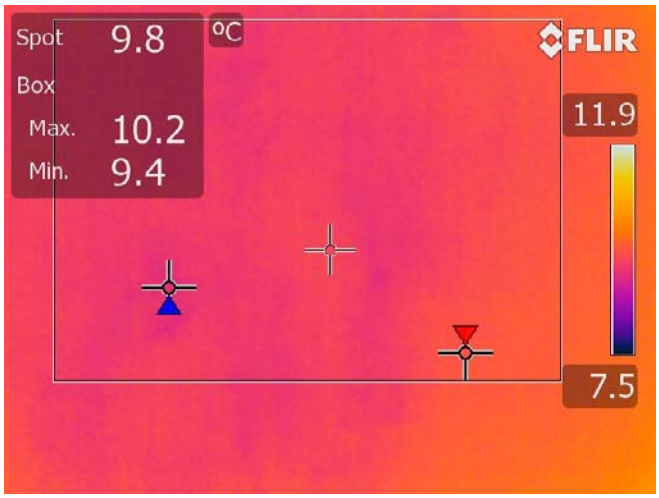

Figure A-24. *IR_0293.jpg, The width of the picture is about 2 m.*

For an air velocity of 0.5 m/s the evaporation rate would be predicted to be between 9 and 12 g/hr/m^2 somewhat influenced by the spot-size

If there were no heat transport from the rock the evaporation would be smaller. The temperature difference would increase and become essentially constant and exceed the observed value of 2.1 °C as seen in Figure A-27.

The above example has illustrated the procedure and also tried to show that there are uncertainties involved in trying to very accurately predict the seepage rate. When this is deemed necessary the "diaper" method can be used. This is facilitated by that the seepage location is well identified from the IR picture.

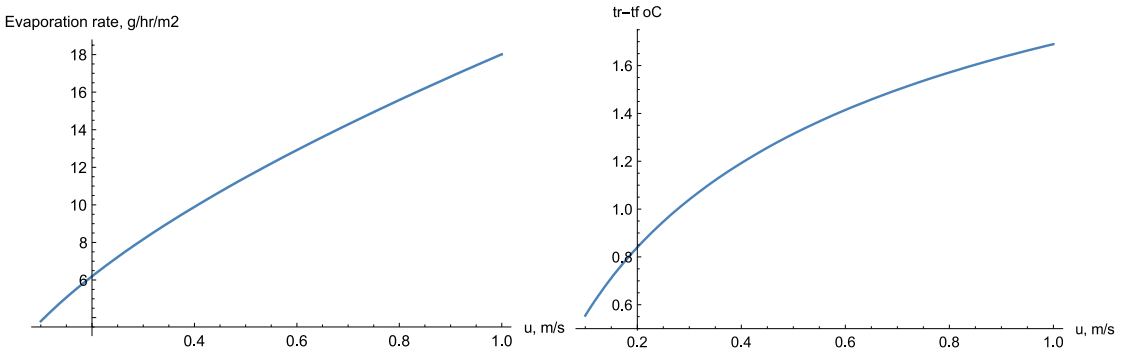

Figure A-25. *Predicted mass flux and temperature difference for r_{Spot} = 1 m. Computer program: Equations for heat and mass transport, evaporation rates and film temperatures.nb)*

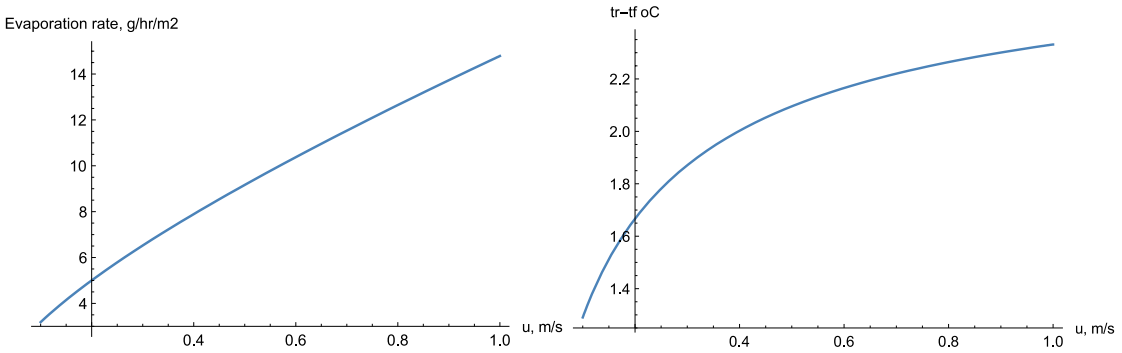

Figure A-26. *Predicted mass flux and temperature difference for $r_{Spot} = r_t\sqrt{2}$ = 3.5 m, i.e. when cylindrical heat conduction is used to describe the contribution from the far away rock. Computer program: Equations for heat and mass transport, evaporation rates and film temperatures.nb)*

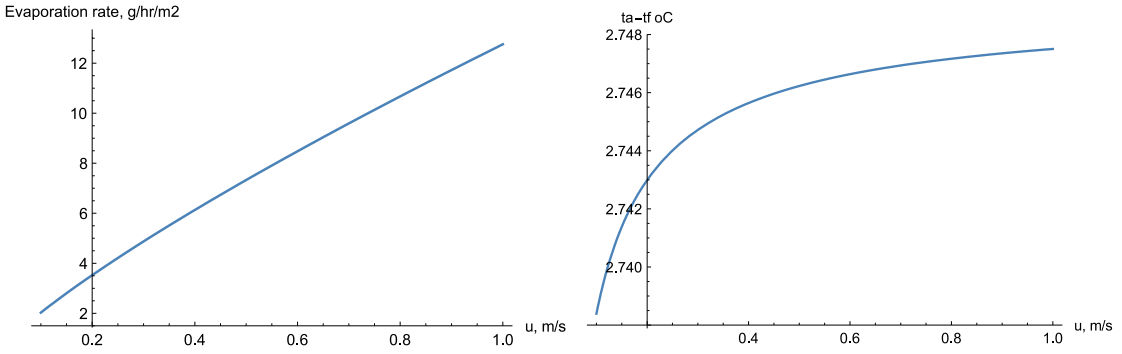

Figure A-27. *Predicted mass flux and temperature difference neglecting heat transport from the rock. Computer program: Equations for heat and mass transport, evaporation rates and film temperatures.nb)*

A.5 Estimation of seepage rate from film velocity

A.5.1 Chapter overview and summary

Flow from channels from which the seeping water is not fully evaporated but flows down the floor and is drained away can be collected in various ways, e.g. by covering the location with a plastic sheet or by the diaper method but could in principle also be derived from the flow velocity of the film pulled downward by gravity. In this chapter we show the underlying theory and equations of it could be as well as how the velocity can be measured by following a dye spot added to the flowing film.

A.5.2 Seepage rate and film velocity

When the cooling film reaches the drain at the side of the floor, the flowrate of water that does not evaporate cannot be determined from the IR pictures as these only give information on the amount that evaporates from the film on the wall. Here we explore if it can be possible to use information on the velocity of the falling film to estimate the flowrate. Then information of the film thickness is needed in addition to the film velocity. The velocity could be measured by adding a tracer at some point and measuring the velocity of the tracer movement. This has been tested on granite slabs but not yet on blasted rock surfaces. Assuming that it works the following approach could be used to estimate the film thickness and obtain the mass flowrate per width of film.

The film thickness is related to the mass flowrate m_{film} per width W by (Bird et al. 2002, p 44 ff)

$$\delta = \sqrt[3]{\frac{3\,\mu_w m_{film}}{\rho_w^2 g W \cos(\beta)}} \tag{A-45}$$

This applies for laminar flow $Re_{film} = \frac{4\delta\rho_w u_f}{\mu_w} < 20$ when rippling is negligible

With the expected flowrates the flow is clearly laminar with Re < 1 and the film thickness is expected to be less than a few hundred μm

The relation between volumetric flowrate $\frac{m_{film}}{W\rho_w}$ $[\frac{m^3}{m\,s}]$ and mean film velocity u_f is

$$\frac{m_{film}}{W\rho_w} = \sqrt{\frac{{u_f}^3 3\mu_w}{\rho_w g \cos(\beta)}} \tag{A-46}$$

or the inverse

$$u_f = \sqrt[3]{(\frac{m_{film}}{W\rho_w})^2 \frac{\rho_w g \cos(\beta)}{3\mu_w}} \tag{A-47}$$

The seepage rate can thus also be assessed by measuring the film velocity. This could be done by inserting a “dot” of dye onto the seeping film and following it as it moves downward. Photographs at intervals can be used to document the movement of the dye. In this way also the seepage rate in regions where the film reaches the drain and stops evaporating can be estimated.

The film velocity is expected to be on the order of a mm/s and less and should be possible to observe. The front of the dye drop travels with 1.5 the mean velocity of the film.

We can relate the flowrate from the channel to its transmissivity if we know the gradient at the wall of the tunnel. In a porous medium this can possibly be measured if the hydraulic head some meters inside the rock is measured. In a fractured rock system with channels in the fractures it is probably difficult to do this in a specific fracture and its channel. We therefore estimate the flow in a channel by modelling the flow as if it were radially converging in a fracture that intersects the tunnel. The flowrate N_w in the fracture with a transmissivity T_w is

$$N_w = T_w \frac{2\pi\Delta H}{ln(\frac{r_{out}}{r_t})} \tag{A-48}$$

The flowrate per metre channel width N_w/W is

$$N_w/W = T_w \frac{\Delta H}{r_t ln(\frac{r_{out}}{r_t})} = \frac{m_{film}}{W\rho_w} \tag{A-49}$$

ΔH is the head difference between a location at a radius r_{out}, and the tunnel radius r_t. We choose the head difference between the tunnel at depth r_{out} = 500 m and that in the tunnel. For a tunnel with radius 2.5 m at 500 m depth ΔH = 500 m and ln (r_{out}/r_t) = 5.3. For this case the (A-49) becomes

$$\frac{m_{film}}{W\rho_w} = 38\, T_w = \sqrt{\frac{{u_f}^3 3\mu_w}{\rho_w g \cos(\beta)}} \qquad \text{(A-50)}$$

With (A-49) we have a relation between the transmissivity and the mass flowrate and thus also between the transmissivity and the film velocity via (A-46). Thus if we can measure the film velocity we can directly obtain the transmissivity of a channel.

With the example of (A-50) the transmissivity of the channel can be assessed by

$$T_w = {u_f}^{3/2} \times \frac{8.5\ 10^{-6}}{\sqrt{\cos(\beta)}}\ [\mathrm{m^2/s}]$$

With u_f in m/s. Note that $u_f = \frac{2}{3}\, u_{f,max}$.

This relation is shown in Figure A-28 for a vertical wall.

A.5.3 Estimation of travel length of film before it evaporates

Figure A-29 gives an example of transmissivities in a location around the so-called feature A at Äspö Hard rock laboratory measured in five boreholes in 0.5 m packed off sections.

Figure A-30 shows the length H_{Film} needed to fully evaporate the water seeping out from channels with different transmissivities and with different air flowrates. The air temperature is 12 °C and the relative humidity 0.5 in this example. The tunnel is located at 500 m depth. The outer head boundary is set to 2.7 r_t. It is seen that for transmissivities larger than 10^{-9} m^2/s high air velocities would be needed to evaporate all the water before it reaches the drain in this example.

In some subsequent practical test at Äspö HRL, shortly described in the main report, it was found to difficult to apply the dye spots and to evaluate the observations.

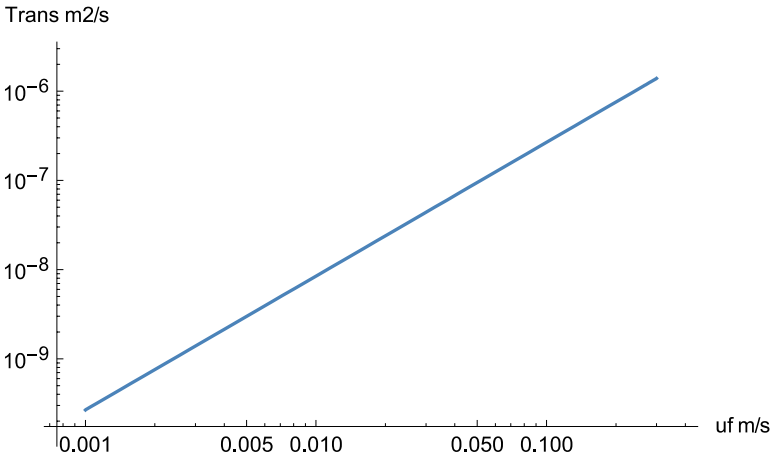

Figure A-28. *Channel transmissivity as function of mean film velocity on a vertical wall in a tunnel at 500 m depth. (Computer program: Flowing film of water.nb)*

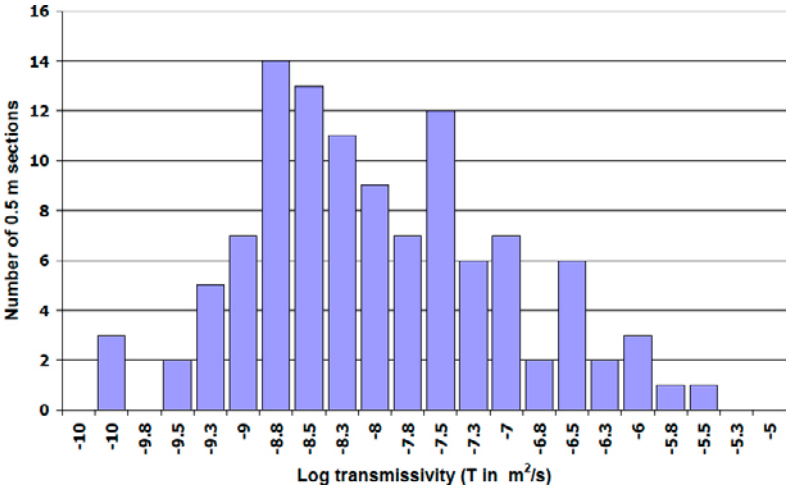

Figure A-29. *Frequency of transmissivities in five boreholes surrounding Feature A at Äspö Hard rock laboratory (Neretnieks 2004).*

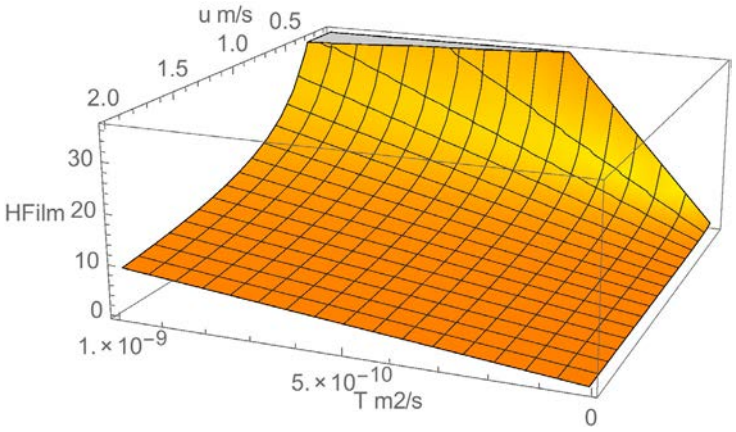

Figure A-30. *Length of water film needed to fully evaporate the water film vs. fracture transmissivity and air velocity. (Computer program: Flowing film of water.nb)*

A.6 Supplementory methods to measure seeping water flowrates from channels

A.6.1 Chapter overview and summary

There is a need to measure the flowrates from seeping channels by some direct method for several reasons. One is to validate the IR based method. Another reason is that for seepage rates that are larger than what can be evaporated, the flowrate of the stream that has not evaporated must be determined. This flow reaches the drain by which it is carried away as liquid water. In this chapter previous experience from a large drift in the Stripa experimental mine are shortly described. Also some scoping experiments in the laboratory are described. However, in some simple scoping tests in the Äspö HRL (TASQ drift) it was not so simple to insert the small dye spots in representative locations and to interpret the results, mostly because of the very uneven velocities of the "falling" film.

A.6.2 Collection by plastic sheets and other direct collection methods

Direct measurement of the flowrate in the drain can be made but then the upstream water must be diverted so that the, often small, additional contribution to the flowrate in the drain can be isolated. Another method is to cover the effluent location identified by the IR picture by a plastic sheet and

collect the water. This is not complicated but the rock surface where the glue is to be applied must be dried first for the glue to stick. The method has been successfully applied on a large scale previously. Nearly 400, 2 m^2 plastic sheets on ceiling and large parts of the walls covered a drift with a total length of 100 m. Water was collected and seepage rates noted over several years (Abelin et al. 1991). Very small flowrates could be accurately monitored. A third method is to cover the seepage location or some convenient downstream area with a piece of cloth or diaper and weigh the mass increase caused by the water uptake of the cloth. Further, in seepage points where the water drips or flows as a free stream it can be collected and the flowrate determined, by the "Bucket and stopwatch" method.

With these methods combined it should be possible to cover the entire range of flowrates expected in the rock that could host a repository.

A.6.3 Scoping experiments to follow film by dye addition

Some simple tests were made to explore if it could be possible to measure flow velocity and flowrate of a moving film of water by addition of small drops of dye. Tests were made in which a moving water film was generated by pouring a small stream of water onto a slightly inclined surface. The water slowly seeps down the inclined surface. A drop of dye is added just downstream of the location where the water is added. The dye drop is followed by taking a film with a digital camera and also by taking a series of pictures with longer intervals at low flow velocities. To facilitate detection a fluorescent dye was used. Ultraviolet light, UV, was used to illuminate the dye. In this way a very tiny amount of dye suffices to clearly follow its progress. When only UV is used for illumination the fluorescence of the dye makes it clearly visible even in very low concentrations.

Figure A-31 shows the setup of the test. A slightly sloping granite slab, 60 × 30 cm, is wetted by a small stream of water from a faucet. The water flows from NW to SE. A drop of uranine solution (Na fluoresciene) is added just downstream of the water from the faucet. Its path is followed by a series of pictures and/or a film sequence. This makes it possible to determine the water velocity along the path. The picture shows the drop of fluoreceine taken under visible light conditions and also when illuminated by only ultraviolet light. This makes the fluoresceine emit visible light. When the visble light is turned off the fluoereceine drop can be followed better. This is shown in the following series of pictures taken at about 1 second intervals.

The pictures in Figure A-32 show the path of the drop illuminated by UV light. The pictures were taken at about 1 second intervals. The flowrate of water was 250 ml /min.

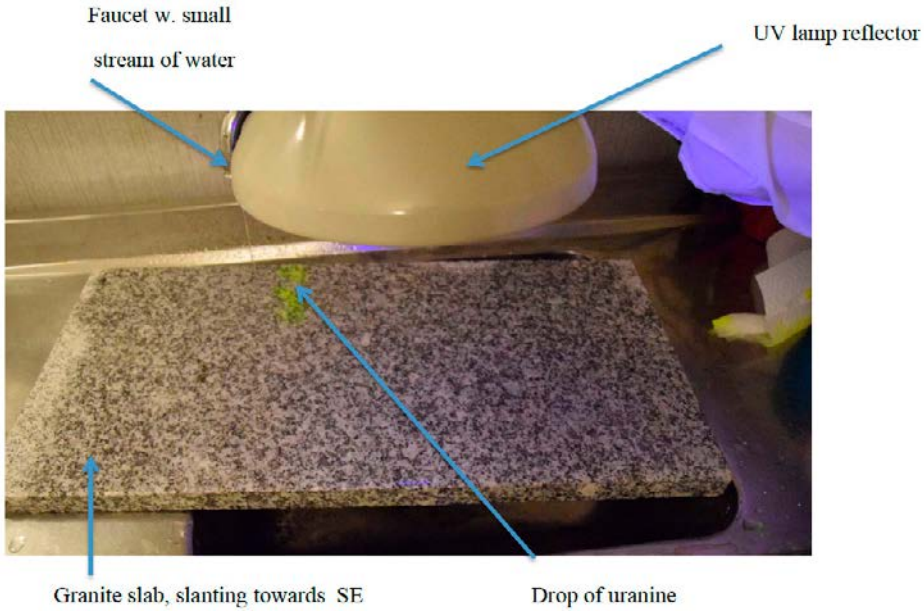

Figure A-31. *Setup of flow velocity detection test device. Flow is from NW to SE.*

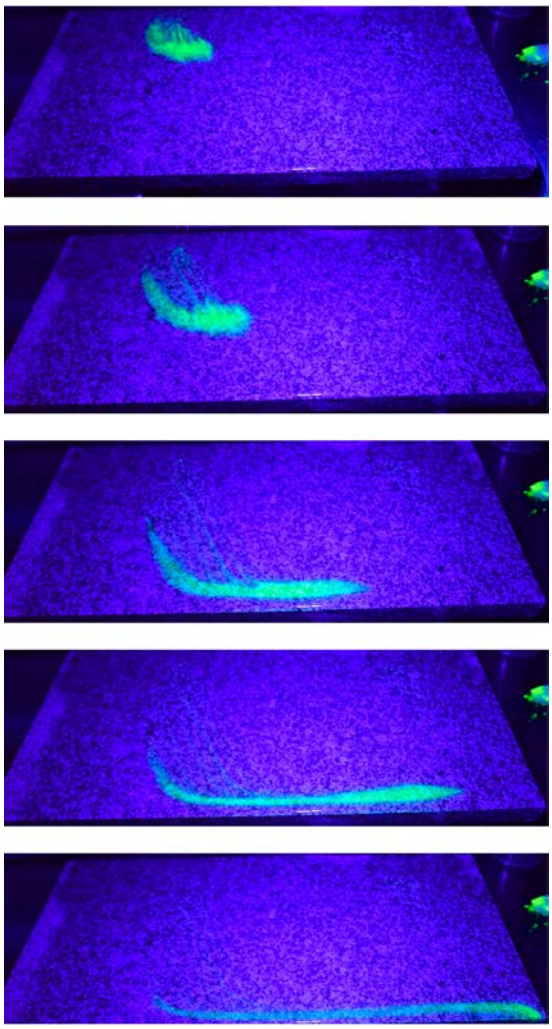

Figure A-32. *A sequence of pictures in UV light of a drop of fluorescein sliding down with the water film on a slightly sloping granite slab. About one second between the frames.*

In the above scoping experiments no effort was made to spread the film evenly over the granite surface. As can be seen from the pictures the water did not flow diagonally but tended to flow first "southwards" until it reached the lower edge of the slab. It did not flow over the edge because of the capillary forces at the sharp edge formed a "barrier". Then the water turned "eastward" and flowed off the slab at the SE corner.

The drop of dye is elongated and a long tail develops because the water velocity perpendicular to the slab's surface rises from zero at the contact of water and solid and develops a parabolic profile upward to the surface of the water film where it has a maximum. The tail forms because the water nearest the solid surface flows with a very small velocity but the water higher up moves more rapidly. The maximum velocity is at the edge of the dye spot and a locally mean velocity and thus flowrate of water can be determined by integration of the velocity profile. The mean velocity is 2/3 that of the maximum.

Another scoping experiment was made outdoors during a light drizzle. The slab was again arranged with slight slope towards SE. The drizzle wetted it more evenly than what could be arranged with the faucet. The wetting rate and thus the film velocity was much lower. The first picture in Figure A-33 shows the slab when the drop of dye just has been emplaced. The second picture shows a frame taken 20 minutes later. The drizzle had then unfortunately just stopped.

The edge of the dye had moved about 10 cm in 20 minutes, which is about 0.3 m/hr. This would be caused by a light rain drizzle of 0.01 mm/hr.

Figure A-33. *Granite slab with moving film generated by slight drizzle. First frame after emplacement of dye drop. Second frame 20 minutes later. Slope of slab is about 5 cm/m.*

These scoping experiments show that the film velocity can be followed simply. By adding several drops on a horizontal line the variations of local flowrates can be obtained.

A.7 Discussion

The whole idea with measuring channel widths, spatial frequencies and flowrate distributions is that this information is needed in channel network models used to simulate and predict radionuclide transport over long times and distances in fractured crystalline rocks hosting a repository for radioactive waste. The repository location will be at a depth of five hundreds of meters and in rock with low transmissivity fractures. It is recognised that water flow takes place in a complex three-dimensional network of channels, many, possibly most of them with low transmissivities. Even low transmissivity channels contribute to the retardation of migrating nuclides. Thus there is a need to obtain data on the channel properties of "all" channels. The IR based technique is a potential way to gather the information needed.

It was shown that IR information can be used to determine the evaporation rate on wet regions and thus to determine the seepage rate from a channel that supplies the water to the cooled area of the rock wall. The method based on IR measurements seems to be robust but must be validated by comparisons with actually measured seepage rates.

It was found that it would be very valuable to have not only individual IR-pictures but to have a simple way of presenting the information in one continuous coherent map of the entire rock surface in the tunnel or drift.

It is recognised that not all water from a channel may have time to evaporate while seeping down the wall when the flowrate is high. Therefore it is important to assess the flowrate of the water that does not evaporate. Several methods can be used. One is to increase the air velocity. A tenfold increase will give 6.3 times higher evaporation rate. Another is to decrease the relative humidity and increase the temperature of the air. A further possibility is to cover the areas with plastic sheets where the IR technique has detected seepage and to collect the water. Another simple way is to collect the seeping water by a cloth that is weighed after some time.

An additional potentially possible method is to measure the velocity of the slowly falling water film in the wet regions by adding small spots of dye that can be visually followed as they migrate downward pulled by gravity. This technique has not been tested yet in a tunnel but could provide a simple way to measure the flowrate from a channel without changing airflow or using plastic sheets or similar techniques.

We beg the reader to recognise that this little report is aimed at exploring the possibilities and especially the limitations of the IR technique by simple scoping calculations. This is a first step to decide if the technique could be useful and should be explored further and possibly implemented. Much work remains.

A.8 Notation

Table A-1. Notation and data used in examples.

Notation	Meaning	Value	Units
$c_{p,a}$	Heat capacity of air	1.04×10^3	J/kg/K Perry and Green 1997 tab 2-198
$c_{p,r}$	Heat capacity of rock	800	J/kg/K
d_t	Diameter of tunnel	5	m
D_{wa}	Vapour diffusion coefficient in air	2.2×10^{-5}	m^2/s P Perry and Green 1997 tab 2-371
D_{ac}	Diffusion coefficient of water by capillary suction		m^2/s
D_T	Thermal diffusion coefficient in rock	1.39×10^{-6}	m^2/s
		43.8	m^2/yr
g	Gravitational constant	9.81	m/s^2
h_a	Heat transfer coefficient for air	$2.9\ u_a^{0.8}$	$W/m^2/K$
H	Height of evaporating film		m
ΔH	Hydraulic head difference		m
ΔH_w	Vaporisation enthalpy of water	2.26×10^6	J/kg
J_{evap}	Mass flux of water due to evaporation		$kg/s/m^2$
J_w	Mass flux of water		$kg/s/m^2$
k_m	Mass transfer coefficient for air	$0.0024\ u_a^{0.8}$	m/s
k_o	Intrinsic permeability of rock matrix		m^2
$k_{rel,w}$	Relative permeability for water		–
K	Hydraulic conductivity	10^{-12}	m/s
m_{evap}	Mass flow of water due to evaporation		kg/s
m_{film}	Mass flow of water in film		kg/s
M_a	Air molar mass	31	kg/kmol
M_w	Water molar mass	18	kg/kmol
N_w	Flowrate of water		m^3/s
p_{va}	Water vapour pressure in air		Pa
p_{vf}	Water vapour pressure at film conditions		Pa
p	Pressure		Pa
Q_a	Heat flow in air		J/s (W)
Q_{evap}	Heat flow by evaporation		J/s (W)
Q_r	Heat flow from rock		J/s (W)
R	Gas constant	8.314	J/mol/K
RH	Relative humidity of air	0.5 and 0.8	–

Notation	Meaning	Value	Units
t	Time		s, yrs
t or T	Temperature	Range 10 to 20 °C	°C, K
T_w	Transmissivity of channel		m^2/s
u_a	Air velocity	0.1–2	m/s
u_f	Water film mean velocity		m/s
W	Width of section		m
β	Angle from vertical	0	
β_m,β_T	Mass and thermal expansion coefficients		–, $kg/m^3/K$
δ	Water film thickness		m
λ_a	Thermal conductivity of air	0.025	W/m/K Perry and Green 1997 tab 2-363
λ_r	Thermal conductivity of rock	3.0	W/m/K
ρ_a	Air density	1.3	kg/m^3
ρ_r	Rock density	2 700	kg/m^3
ρ_v	Water vapour density		kg/m^3
ρ_w	Water density	1 000	kg/m^3
μ_w	Water viscosity	0.001	Pa × s
Subscripts			
a	Air		
f	Film		
r	Rock		
v	Water vapour		
w	Liquid water		

Arkitektkopia AB, Bromma, 2018

SKB is responsible for managing spent nuclear fuel and radioactive waste produced by the Swedish nuclear power plants such that man and the environment are protected in the near and distant future.

skb.se